Multiobjective Multidisciplinary Optimization of Low-Boom Supersonic Transports Using Multifidelity Models

Wu Li[*] and Karl Geiselhart[†]

NASA Langley Research Center, Hampton, Virginia 23681, USA

   A multidisciplinary optimization (MDO) method has been developed to design a computational fluid dynamics (CFD) based low-boom configuration that can be obtained from a Pareto solution of a low-fidelity multiobjective MDO problem with mission constraints. This paper refines the developed MDO method by using multifidelity models for CFD-based multiobjective MDO and a better method for the system-level trade between the target low boom ground noise level and the overland range. The refined MDO method can generate a low-boom configuration that satisfies the mission requirements, has the lowest takeoff gross weight and the longest range for the low-boom mission, trims the low-boom cruise flight with fuel redistributions, and has a reversed equivalent area distribution closely matching a low-boom target with ground noise level below 70 PLdB. The validity of the refined MDO method is demonstrated by a design study of a low-boom supersonic transport that carries 40 passengers, flies a low-boom mission with cruise Mach of 1.7 and range of 3500 nm, and cruises overwater at Mach 1.8 with range of 3882 nm. Moreover, the refined MDO method eliminates the difference between the assumed cruise weight for CFD-based low-boom inverse design optimization and the estimated cruise weight of the optimal inverse design solution with respect to the mission requirements.

Nomenclature

$\lVert \cdot \rVert_k$	=	$\lVert \cdot \rVert_{k,l_e}$, k-norm of a function on interval $[0, l_e]$
$\lVert \cdot \rVert_{k,\lambda}$	=	k-norm of a function f on interval $[0, \lambda]$ defined by $\lVert f \rVert_{k,\lambda}$, which equals $\left(\frac{1}{\lambda}\int_0^\lambda |f(t)|^k \, dt\right)^{\frac{1}{k}}$
A_e	=	any equivalent area including $A_{e,m}$, $A_{e,LoFi}$, $A_{e,MuFi}$, $A_{e,CFD}$, and $A_{e,r}$, ft^2
$A_e^{''}$	=	second derivative of A_e with respect to x_e
$A_e(\boldsymbol{D})$	=	A_e for $\boldsymbol{D}$, ft^2
$A_e(x_e, \boldsymbol{D})$	=	A_e value at x_e for $\boldsymbol{D}$, ft^2
$A_{e,CFD}$	=	$A_{e,m}$ computed using CFD lift distribution, ft^2
$A_{e,LoFi}$	=	$A_{e,m}$ computed using low-fidelity aero lift distribution, ft^2
$A_{e,MuFi}$	=	multifidelity model for approximation of $A_{e,r}$, ft^2
$A_{e,m}$	=	classical equivalent area defined by Mach angle cut method, ft^2
$A_{e,r}$	=	reversed equivalent area defined by using reverse propagation of CFD off-body pressure, ft^2
$A_{e,CFD}^{lift}$	=	lift part of $A_{e,CFD}$, which equals $A_{e,CFD}^{lift} + A_{e,CFD}^{volume}$, ft^2
$A_{e,LoFi}^{lift}$	=	lift part of $A_{e,LoFi}$, which equals $A_{e,LoFi}^{lift} + A_{e,LoFi}^{volume}$, ft^2
$A_{e,MiFi}^{lift}$	=	A_e due to lift computed using the calibrated lift method, ft^2
$A_{e,MuFi}^{lift}$	=	multifidelity model for approximation of $A_{e,CFD}^{lift}$, ft^2
$A_{e,r}^{target}$	=	$A_{e,r}$ target for $\boldsymbol{D}$, ft^2
$A_{e,r,0}^{target}$	=	$A_{e,r}$ target for $\boldsymbol{D}_0$, ft^2
$A_{e,CFD}^{volume}$	=	volume part of $A_{e,CFD}$, which equals $A_{e,CFD}^{lift} + A_{e,CFD}^{volume}$, ft^2
$A_{e,LoFi}^{volume}$	=	volume part of $A_{e,LoFi}$, which equals $A_{e,LoFi}^{lift} + A_{e,LoFi}^{volume}$, ft^2
CG_x	=	longitudinal center of gravity, ft
$CG_{x,aft}$	=	most aft CG_x at start of overland cruise using fuel redistribution for $\boldsymbol{D}$, ft

[*] Senior Research Engineer, Aeronautics Systems Analysis Branch
[†] Aerospace Engineer, Aeronautics Systems Analysis Branch

$C_L(\boldsymbol{D}_{\mathrm{LoW}})$ = lift coefficient of $\boldsymbol{D}_{\mathrm{LoW}}$ at start of overland cruise

CP_x = longitudinal center of pressure, ft

$\mathrm{CP}_{x,\mathrm{CFD}}$ = computational fluid dynamics CP_x for $\widehat{\boldsymbol{D}}$, ft

$\boldsymbol{D}$ = vector of $\boldsymbol{d}_{\mathrm{tgt}}$, $\boldsymbol{d}_{\mathrm{frt}}$, $\boldsymbol{d}_{\mathrm{wing}}$, $\boldsymbol{d}_{\mathrm{aft}}$, $\boldsymbol{d}_{\mathrm{LTO}}$, θ_{htail}, F_{s}, R_{OL}, and H_{OL}

$\widehat{\boldsymbol{D}}$ = independent copy of $\boldsymbol{D}$ with θ_{htail} and $\boldsymbol{d}_{\mathrm{aft}}$ replaced by $\widehat{\theta}_{\mathrm{htail}}$ and $\widehat{\boldsymbol{d}}_{\mathrm{aft}}$, respectively

$\boldsymbol{D}_0$ = $\boldsymbol{D}$ for baseline

$\widehat{\boldsymbol{D}}_{\mathrm{aft}}$ = $\widehat{\boldsymbol{D}}$ for solution of CFD-based low-boom aft shaping of $\boldsymbol{D}_{\mathrm{MaxR}}$

$\boldsymbol{d}_{\mathrm{aft}}$ = vector of design variables for locations and incident angles of pylon and nacelle

$\widehat{\boldsymbol{d}}_{\mathrm{aft}}$ = independent copy of $\boldsymbol{d}_{\mathrm{aft}}$ for $\widehat{\boldsymbol{D}}$

$\boldsymbol{d}_{\mathrm{frt}}$ = vector of widths, heights, and locations for fuselage cross sections

$\boldsymbol{D}_{\mathrm{fs}}$ = $\boldsymbol{D}$ for feasible low-boom design

$\boldsymbol{D}_{\mathrm{id}}$ = $\boldsymbol{D}$ for ideal low-boom design

$\widehat{\boldsymbol{D}}_{\mathrm{LoT}}$ = previously documented CFD-based low-boom design

$\boldsymbol{D}_{\mathrm{LoW}}$ = $\boldsymbol{D}$ for the lowest weight solution on the Pareto frontier of multiobjective MDO, which also has an acceptable matching error for low-boom inverse design (i.e., $\left\| A_{\mathrm{e,MuFi}}(\boldsymbol{D}) - A_{\mathrm{e,r}}^{\mathrm{target}}(\boldsymbol{D}) \right\|_{k,\lambda} \leq \varepsilon$)

$\boldsymbol{d}_{\mathrm{LTO}}$ = vector of 6 auxiliary design variables for landing and takeoff: flap deflection angles, main gear length, and CG_x offsets for trim at landing and takeoff

$\boldsymbol{D}_{\mathrm{MaxR}}$ = $\boldsymbol{D}$ for plausible low-boom design with maximum overland range

$\widehat{\boldsymbol{D}}_{\mathrm{MaxR}}$ = $\widehat{\boldsymbol{D}}$ obtained with replacing θ_{htail} of $\boldsymbol{D}_{\mathrm{MaxR}}$ by appropriate $\widehat{\theta}_{\mathrm{htail}}$

$\boldsymbol{d}_{\mathrm{tgt}}$ = vector of 12 control-point coordinates of Bezier parametric curve for $A_{\mathrm{e,r,0}}^{\mathrm{target}}$ or $A_{\mathrm{e,r}}^{\mathrm{target}}$

$\boldsymbol{d}_{\mathrm{wing}}$ = vector of 15 wing design variables

F_{s} = sea-level static thrust for engine, lb

$\widehat{F}_{\mathrm{s}}$ = independent copy of F_{s} as input for the Numerical Propulsion System Simulation, lb

$F(t)$ = F-function for A_{e}

g_i = constraint function for mission constraint (II.i) computed using the calibrated lift method

H_{OL} = cruise altitude for overland mission or for CFD analysis, ft

k = positive integer to define integral of matching error for low-boom inverse design optimization

l = lower-bound vector for $\boldsymbol{D}$ or $\widehat{\boldsymbol{D}}$

L/D = lift-to-drag ratio

l_{e} = effective length of configuration defined by $\boldsymbol{D}$, which is the largest effective distance where Mach angle cut plane intersects the configuration, ft

$l_{\mathrm{e},0}$ = l_{e} for $\boldsymbol{D}_0$, ft

M_{OL} = cruise Mach number for overland mission

MTOGW = maximum of $\mathrm{TOGW}_{\mathrm{OL}}$ and $\mathrm{TOGW}_{\mathrm{OW}}$, lb

p = longitudinal pressure distribution at undertrack location below aircraft, $\mathrm{lb/ft}^2$

p_∞ = ambient pressure, $\mathrm{lb/ft}^2$

$\mathrm{PLdB}(A_{\mathrm{e}})$ = perceived level in decibels of sonic boom ground signature for A_{e}

r = distance from undertrack location to aircraft, ft

R_{OL} = range for overland mission, nm

$S_{\mathrm{ref}}(\boldsymbol{D}_{\mathrm{LoW}})$ = wing reference area of $\boldsymbol{D}_{\mathrm{LoW}}$ for calculation of lift coefficient, ft^2

t = temporary variable

$\mathrm{TOGW}_{\mathrm{OL}}$ = takeoff gross weight for overland mission of $\boldsymbol{D}$, lb

$\mathrm{TOGW}_{\mathrm{OW}}$ = takeoff gross weight for overwater mission of $\boldsymbol{D}$, lb

u = upper-bound vector for $\boldsymbol{D}$ or $\widehat{\boldsymbol{D}}$

U_∞ = freestream velocity at cruise altitude H_{OL}, ft/sec

W_{crs} = weight at start of overland cruise for $\boldsymbol{D}$, lb

x, y, z = coordinates of point in space, ft

x_{e} = effective distance for A_{e}, ft

$\widehat{x}_{\mathrm{e}}$ = effective distance computed using piecewise linear transformation of x_{e}, ft

$x_{\mathrm{e,tte}}$ = x_{e} location corresponding to tailing edge of wing tip airfoil, ft

$x_{\mathrm{e}}(\boldsymbol{D})$ = a specific x_{e} location related to $\boldsymbol{D}$ such as $x_{\mathrm{e,tte}}(\boldsymbol{D})$, ft

y_i = y coordinate of span location of wing, ft

y_{rt} = calibration parameter for span location to truncate wing for low-fidelity aero analysis, ft

α = angle of attack at start of overland cruise for $\boldsymbol{D}$, deg

α_{LoW} = angle of attack at start of overland cruise for $\boldsymbol{D}_{\mathrm{LoW}}$, deg

β	=	Prandtl-Glauert factor $\sqrt{(M_{OL})^2 - 1}$
γ	=	ratio of specific heats
$\Delta A_{e,CFD}^{lift}$	=	correction term for $A_{e,CFD}^{lift}$, ft^2
$\Delta A_{e,r}$	=	correction term for $A_{e,r}$, ft^2
δ	=	lower bound for trim ratio $A_{e,r,0}^{target}(l_{e,0}/2)/A_{e,r,0}^{target}(l_{e,0})$
ε	=	tolerance of $0.007 \cdot A_{e,r}^{target}(l_e)$ for acceptable low-boom inverse design objective value
θ_{htail}	=	deflection angle of an all-moving horizontal tail at start of overland cruise for $\boldsymbol{D}$, deg
$\hat{\theta}_{htail}$	=	independent copy of θ_{htail} for $\hat{\boldsymbol{D}}$, deg
θ_Δ	=	calibration parameter for θ_{htail} of $\boldsymbol{D}$, deg
λ	=	$l_e \cdot \lambda_0/l_{e,0}$, upper limit for integration of A_e matching error for $\boldsymbol{D}$, ft
λ_0	=	x_e location of the highest point on $A_{e,LoFi}(\boldsymbol{D}_0)$ or $l_{e,0}$, ft
μ	=	ratio $A_{e,r}^{target}(l_e)/A_{e,CFD}(l_e)$ as estimate of $A_{e,r}(l_e)/A_{e,CFD}(l_e)$ for expected low-boom design
ρ_∞	=	ambient density at cruise altitude H_{OL}, lb/ft^3
$\tau_{i,max}$	=	design section lift coefficient for NACA 63-series airfoil at span location y_i
τ_{max}	=	design section lift coefficient for NACA 63-series airfoil

I. Introduction

T HE Shaped Sonic Boom Demonstration (SSBD) program [1] validated via flight testing that the shaping benefits of a modified F-5E aircraft could be maintained through the atmosphere to achieve a flat-top front ground signature as predicted using computational methods {see fig. 26 in Ref. [1]}. The NASA X-59 low-boom flight demonstrator (LBFD) [2] aims to achieve a greatly reduced ground noise level of sonic boom under cruise conditions and paves the way for commercial supersonic overland flight. The LBFD project will help determine future Federal Aviation Administration (FAA) regulations on the acceptable ground noise level for supersonic overland flight and validate sonic boom prediction methods. The current NASA low-boom requirement is based on the perceived level in decibels (PLdB [3]) of the sonic boom ground signature. The NASA N+3 goal [4,5] for the acceptable sonic boom level is below 70 PLdB.

The studies of low-boom configurations start with the George-Seebass-Darden (GSD) boom minimization theory, which treats a supersonic wing-body configuration as a body of revolution [6,7] and generates optimal F-functions [8,9] for shaping the equivalent area ($A_{e,m}$) distributions of low-boom configurations. The GSD low-boom F-functions are used in most pre-SSBD low-boom design studies. Various extensions of the GSD F-functions have been proposed to accommodate more complex nearfield shock wave patterns of low-boom supersonic configurations [10-13]; and a low-boom F-function for an aft A_e bump [14] was developed to enable a forward shift of lift distribution and achieve the low-boom cruise trim without control surface deflections. The most advanced boom minimization study [15] based on the body-of-revolution approximation is to match the CFD-based equivalent area ($A_{e,CFD}$) with a low-boom A_e target generated using the F-function form in Ref. [11] for a wing-body configuration. The low-boom shaping based on the body-of-revolution approximation is useful to attain a low-boom front shape of the ground signature such as the flat-top ground signature of the SSBD demonstrator [1]. Interested readers should refer to Ref. [16] for a comprehensive documentation of sonic boom research up until 2013.

The ground signature propagated from $A_{e,CFD}$ [the computational fluid dynamics (CFD) body-of-revolution approximation form of a three-dimensional supersonic aircraft] has a very different aft shape when compared to the signature propagated from CFD off-body pressure, even for a wing-body configuration {see fig. 2 in Ref. [17]}. The current state-of-the-art sonic boom analysis [18,19] uses CFD off-body pressure at a location at least three body lengths away from the aircraft and propagates the off-body pressure through the atmosphere using an augmented Burgers equation [20,21] to get the ground signature. For convenience, such a ground signature will be called *CFD-based ground signature*. The NASA N+3 low-boom goal is to develop a supersonic transport concept that has a CFD-based ground signature with noise level below 70 PLdB. To date, this goal has not been achieved computationally by any supersonic concept. The NASA X-59 LBFD is expected to attain a CFD-based ground signature with noise level about 75 PLdB.

CFD-based low-boom inverse design optimization methods [17,22-25] are capable of generating supersonic configurations with nacelles that yielded CFD-based ground signatures with noise levels below 79 PLdB. The undertrack ground noise levels for the optimized supersonic configurations are about 78.5 PLdB for mixed-fidelity inverse design optimization of reversed equivalent area $A_{e,r}$ [17,25] and about 76.3 PLdB for adjoint-based inverse design optimization methods [22-24]. For a wing-body configuration, a CFD-based ground signature with noise level of 78.9 PLdB was attained [26] using inverse design optimization of $A_{e,r}$.

One undesirable consequence of low-boom inverse design optimization is that the resulting low-boom configuration might have a much lower L/D value at the start of low-boom cruise than anticipated. As a result, the low-boom configuration might only be able to fly a shorter range than required. This is not a problem for a low-boom flight demonstrator such as the NASA X-59 LBFD, which only requires to fly enough distance for ground measurements of sonic boom signatures and noise levels. However, for a commercial low-boom supersonic aircraft, a shorter range than required might be unacceptable. Moreover, a commercial low-boom supersonic aircraft must be able to take off, cruise, and land for the intended origin-destination pairs of airports. This requires multiobjective multidisciplinary optimization (MDO) of low-boom supersonic aircraft.

The Quiet Supersonic Platform program [27] initiated the research on multiobjective MDO of low-boom supersonic aircraft. Most low-boom MDO studies simultaneously optimize a sonic boom objective and some performance metrics. The sonic boom objectives include the shock strength [28,29] (i.e., the sum of shock jumps within a short time span such as a few milli-seconds at the start of the ground signature), maximum value/magnitude [30-32] or range [33-35] of the overpressure on the ground, and dBA [36] or PLdB [10] of the ground signature. The performance metrics include various drag coefficients [29,30,32-34], lift coefficient [33], L/D [10,31,35], wing structural weight [33-35], maximum takeoff gross weight (MTOGW) [28,36], range [28], and trim for low-boom cruise [34]. While these optimization studies are performed for a variety of specific design cases, a consensus from these studies is that a severe penalty on performance is unavoidable when optimizing a sonic boom objective. See Ref. [37] for a review of MDO applied to sonic boom minimization.

The separation of low-boom inverse design optimization and low-boom MDO is not accidental. An inverse design objective in low-boom MDO could make the resulting optimization problem unsolvable due to the implicit requirement of the inverse design optimization: the optimal inverse design objective value must be close to zero for an acceptable inverse design solution. Drag reduction coupled with an inverse design objective is only used to refine an existing low-boom baseline [38,39]. Two configurations with low-boom front A_e shapes are optimized for drag reduction by modifying the upper side of the fuselage [38]. The result shows that a reduction of the drag coefficient is achieved with a significant deviation of the front A_e shape away from the low-boom target {see fig. 12 in Ref. [38]}. Another drag reduction study of a low-boom baseline minimizes a weighted average of the drag and a low-boom inverse design objective [39]. The baseline is the Lockheed Martin N+2 low-boom concept. The drag is reduced by 3%, while A_e deviates at most 2% from the target.

The recent attempts [40,41] of integrating a low-boom inverse design objective in multiobjective low-boom MDO used inverse design objectives of various fidelities, which led to low-boom concepts under different fidelity assumptions. To clarify different fidelities of low-boom concepts for inverse design optimization, three qualifiers are introduced. For any design vector $\boldsymbol{D}$, $\boldsymbol{D}$ is called a *plausible* low-boom design with 70 PLdB if $\|A_{e,m}(\boldsymbol{D})-A_{e,r}^{\text{target}}\|_{k,\lambda} \leq \varepsilon$ and $\text{PLdB}(A_{e,r}^{\text{target}}) = 70$; $\boldsymbol{D}$ is called a *feasible* low-boom design with 70 PLdB if $\|A_{e,r}(\boldsymbol{D}) - A_{e,r}^{\text{target}}\|_{k} \leq \varepsilon$ and $\text{PLdB}(A_{e,r}^{\text{target}}) = 70$; and $\boldsymbol{D}$ is called an *ideal* low-boom design with 70 PLdB if $\text{PLdB}(A_{e,r}(\boldsymbol{D})) = 70$. The parameter $\varepsilon = 0.007 \cdot A_{e,r}^{\text{target}}(l_e)$ determines the acceptable error tolerance for inverse design optimization, and it can be replaced by any relatively small number. The target PLdB value of 70 can also be replaced by another ground noise limit (such as 69.9) in these definitions. The equivalent area $A_{e,m}(\boldsymbol{D})$ in the definition of the plausible low-boom design could be replaced by other approximation forms of $A_{e,r}(\boldsymbol{D})$. To make a plausible low-boom design useful in practice, $A_{e,m}(\boldsymbol{D})$ must not be drastically different from $A_{e,r}(\boldsymbol{D})$ over the interval $[0, \lambda]$ so that minor modifications of $\boldsymbol{D}$ could lead to a feasible low-boom design. In this paper, λ is a location just ahead of the nacelles to ensure that a plausible low-boom design does have approximately a low-boom front shape up to the effective distance location of λ. A feasible low-boom design has an approximately perfect low-boom shape, but its undertrack ground signature could have a much higher PLdB value than the target value of 70 PLdB. The ground signature of $A_{e,r}$ is almost identical to that of the off-body pressure used to compute $A_{e,r}$ and the PLdB values of these two ground signatures are about the same {see fig. 4 in Ref. [17]}. So, $\text{PLdB}(A_{e,r}(\boldsymbol{D}))$ accurately represents the noise level of the CFD-based ground signature of $\boldsymbol{D}$. An ideal low-boom design is a feasible low-boom design with the inverse design matching error of zero. It has the perfect low-boom shape that has an undertrack ground signature with 70 PLdB. The NASA N+3 low-boom goal can be restated as an ideal low-boom design with PLdB less than 70, which has not been realized yet. However, it is possible to find a feasible low-boom design with PLdB less than 70 that also satisfies the mission requirements, which is a significant step moving toward the required ideal low-boom design as shown below.

The mathematical theory for a feasible low-boom design as an accurate approximation of an ideal low-boom design is based on an approximation relationship [42] between $A_{e,\text{CFD}}$ and $A_{e,r}$.

$$A_{e,\text{CFD}}(x_e, \boldsymbol{D}_{\text{fs}}) - A_{e,\text{CFD}}(x_e, \boldsymbol{D}_{\text{id}}) \approx A_{e,r}(x_e, \boldsymbol{D}_{\text{fs}}) - A_{e,r}(x_e, \boldsymbol{D}_{\text{id}}) \quad \text{for } 0 \leq x_e \leq l_e \tag{1}$$

Assume that $\boldsymbol{D}_{fs}$ is a feasible low-boom design and its low-boom target $A_{e,r}^{target}$ is perfectly matched by an ideal low-boom design $\boldsymbol{D}_{id}$. Then it follows from Eq. (1) and $A_{e,r}(\boldsymbol{D}_{id}) = A_{e,r}^{target}$ that

$$\left\|A_{e,CFD}(\boldsymbol{D}_{fs}) - A_{e,CFD}(\boldsymbol{D}_{id})\right\|_k \approx \left\|A_{e,r}(\boldsymbol{D}_{fs}) - A_{e,r}(\boldsymbol{D}_{id})\right\|_k = \left\|A_{e,r}(\boldsymbol{D}_{fs}) - A_{e,r}^{target}\right\|_k \leq \varepsilon \qquad (2)$$

The last inequality in Eq. (2) follows from the definition of $\boldsymbol{D}_{fs}$ as a feasible low-boom design. Equation (2) implies that the ideal low-boom design (if it exists) could be obtained with minor modifications of $A_{e,CFD}(\boldsymbol{D}_{fs})$. That is, an ideal low-boom design could be obtained with minor volume and lift modifications of $\boldsymbol{D}_{fs}$. So, a feasible low-boom design is not too far away from an ideal low-boom design (if it exists) when the matching error between their $A_{e,CFD}$ distributions is used as the distance metric. Moreover, it can be used as the starting point to generate an ideal low-boom design using an adjoint-based low-boom design method. A feasible low-boom design with PLdB less than 70 that also satisfies the mission requirements will bring the NASA N+3 low-boom goal closer to reality.

Now, the progresses from the previous low-boom MDO studies to the present one can be summarized as a march toward the NASA N+3 low-boom goal. The first design study is a plausible low-boom design with 68.4 PLdB that also satisfies the mission requirements [40]. The corresponding multiobjective MDO problem minimizes the inverse design objective $\|A_{e,LoFi}(\boldsymbol{D}) - A_{e,r}^{target}\|_{k,\lambda}$ and MTOGW with the specified mission constraints.

The follow-up study [41] adds a system-level trade method to optimize the cruise Mach, cruise altitude, and range for the low-boom overland mission, and increases the fidelity of the inverse design objective. The resulting multiobjective MDO problem seeks a Pareto solution for minimum $\|A_{e,r}(\boldsymbol{D}) - A_{e,r}^{target}\|_2$, minimum MTOGW, maximum overland cruise Mach, and maximum overland range, while satisfying the mission constraints. The generated solution using a block coordinate optimization (BCO) method was a feasible low-boom design with 69.9 PLdB as defined above. This feasible low-boom design was obtained from a plausible low-boom design with minor wing modifications, while the plausible low-boom design satisfies the mission requirements. This is very close to the goal of finding a feasible low-boom design with PLdB less than 70 that also satisfies the mission requirements. The minor wing differences between the feasible and plausible low-boom designs are caused by the discrepancies between the CFD analysis for low-boom inverse design optimization and low-fidelity aero analyses for low-fidelity multiobjective MDO.

This paper achieves the goal of obtaining a feasible low-boom design with 69.9 PLdB that also satisfies the mission requirements. The block coordinate optimization (BCO) method in Ref. [41] is refined with the following two improvements: 1) using multifidelity models to eliminate the discrepancies between the low-fidelity aero and CFD analyses, and 2) developing a better method for the system-level trade between the target low-boom ground noise level and range for the low-boom overland mission. The MTOGW and ranges of this feasible low-boom design are all better than those in Ref. [41], with a compromise of reducing the low-boom cruise Mach from 1.8 to 1.7. See Table 1 for a comparison of these three concepts.

Table 1 Comparison of three low-boom concepts

	Plausible low-boom design [40]	Approximate feasible low-boom design [41]	Feasible low-boom design (in this paper)
Number of passengers	40	40	40
Seat pitch, in	48	48	48
MTOGW, lb	154,474	145,164	144,251
Overwater cruise Mach	1.8	1.8	1.8
Overwater range, nm	3600	3600	3882
Low-boom cruise Mach	1.6	1.8	1.7
Low-boom range, nm	2500	2950	3500
Low-boom cruise altitude, ft	45,000	50,700	52,240
Target PLdB	68.8	69.5	69.9
CFD L/D for low-boom cruise	—	8.9	10.1

The paper is organized as follows. Section II introduces the CFD-based multiobjective MDO problem for design of low-boom supersonic transports and the refined BCO method. Section III demonstrates that the refined BCO

method can generate a feasible low-boom design with 69.9 PLdB that also satisfies the mission requirements. Concluding remarks are given in Sec. IV.

II. Block Coordinate Optimization Using Multifidelity Models

A CFD-based multiobjective MDO problem and its solution method are formulated to find a feasible low-boom design with 70 PLdB that also satisfies the mission requirements. Section II.A includes the baseline geometry and design variables for solving the multiobjective MDO problem. A calibrated lift method for low-boom MDO is developed in Sec. II.B. The calibrated lift method allows the low-fidelity aero analysis code LTSTAR [43] to reproduce the CFD wing lift and CFD total lift at the start of overland cruise. This method uses a truncated and shifted wing geometry and a calibrated tail rotation angle for the LTSTAR analysis. The mission performance metrics can be computed using low-fidelity aero analysis codes applied on the same truncated and shifted wing geometry and the horizontal tail at the calibrated tail rotation angle. These mission performance metrics are used to define the CFD-based multiobjective MDO problem in Sec. II.C. To save computational costs, multifidelity models are constructed in Sec. II.D to solve the CFD-based multiobjective MDO problem. The BCO method in Ref. [41] is refined in Sec. II.E with a better trade method for the maximum overland range and a higher fidelity low-boom MDO solution using the multifidelity models. The implementation details for the refined BCO method are provided in Sec. II.F. The validity of the refined BCO method will be demonstrated using a numerical example in Sec. III.

A. Baseline and Design Variables for BCO

The feasible low-boom solution with 69.9 PLdB in Ref. [41] was labeled as $\widehat{\boldsymbol{D}}_{\text{LoT}}$. It was used to test and debug the refined BCO method. After the refined BCO method has been implemented correctly, the resulting feasible low-boom design is denoted by $\widehat{\boldsymbol{D}}_{\text{aft}}$. The initial baseline (see Fig. 1) for the refined BCO method is denoted by $\boldsymbol{D}_0$, which only differs from $\widehat{\boldsymbol{D}}_{\text{aft}}$ by a difference of 4.166° in the tail deflection angle. The engine thrust of 36,000 lb for $\widehat{\boldsymbol{D}}_{\text{LoT}}$ [41] was reduced to 34,000 lb for $\boldsymbol{D}_0$ during this design exploration process. The pylon, horizontal tail, and vertical tail of $\widehat{\boldsymbol{D}}_{\text{LoT}}$ are inherited by $\boldsymbol{D}_0$. The horizontal tail area is 388 ft^2 and the vertical tail area is 266 ft^2, which are fixed in this paper. Some specifications of the baseline are listed in Table 2.
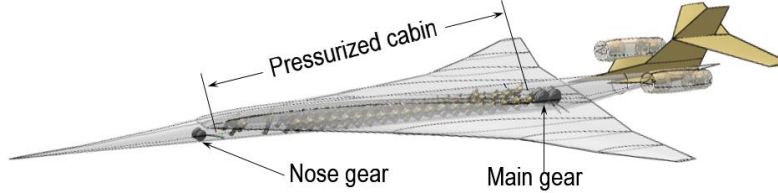

Fig. 1 Cabin arrangement and main gear packaging for initial baseline.

Table 2 Specifications of the baseline

Overwater cruise Mach	1.8	Overland cruise Mach	1.7
Overwater cruise range, nm	3600	Overland cruise range, nm	2500
Overwater takeoff gross weight, lb	120,486	Overland takeoff gross weight, lb	138,904
Zero fuel weight, lb	70,776	Low-boom cruise altitude, ft	56,200

The design vector $\boldsymbol{D}$ has $\boldsymbol{d}_{\text{frt}}$, $\boldsymbol{d}_{\text{wing}}$, $\boldsymbol{d}_{\text{aft}}$, $\boldsymbol{d}_{\text{LTO}}$, $\boldsymbol{d}_{\text{tgt}}$, θ_{htail}, F_{s}, R_{OL}, and H_{OL} as its components. The partition of $\boldsymbol{D}$ into weakly coupled blocks of design variables is important for low-boom MDO {see Refs. [40,41]}. The subvector $\boldsymbol{d}_{\text{frt}}$ consists of the design variables of the fuselage to define a low-boom front shape. The subvector $\boldsymbol{d}_{\text{wing}}$ has the wing design variables, which define the low-boom shape in the midrange of effective distance. The subvector $\boldsymbol{d}_{\text{aft}}$ has the design variables for the aft components and determines the low-boom aft shape. The subvectors $\boldsymbol{d}_{\text{LTO}}$ and $\boldsymbol{d}_{\text{tgt}}$ contain the design variables for landing and takeoff (LTO) performance and low-boom target $A_{\text{e,r}}^{\text{target}}$, respectively. The tail rotation angle θ_{tail} determines the appropriate ratio between the wing lift and horizontal tail lift for a low-boom configuration. The engine thrust F_{s} is a design variable to find the most efficient engine to complete the overland and overwater missions. The overland cruise altitude H_{OL} is a design variable for an optimal trade between the sonic boom noise level on the ground and the cruise efficiency for the overland mission. The overland cruise Mach M_{OL} is not a design variable and its fixed value of 1.7 is empirical.

The design variables for span locations of the wing sections in Ref. [41] are not used in this paper, while the number of design variables for the fuselage is increased for a more accurate low-boom front shape. The fuselage and wing are reparametrized as follows. The locations, widths, and heights at five cross sections for the front fuselage

shape (see the 13 blue variables in Fig. 2) are used as design variables (d_{frt}) for BCO. The wing has the same parametric planform as in Ref. [41]. However, the span locations are fixed and only 5 design variables (see the blue variables in Fig. 3) are used to change the planform. A design lift parameter $\tau_{\max}$ {i.e., the parameter CLI in the computer code to generate NACA 63-series airfoils [44]} is used to parameterize each NACA 63-series airfoil. Four parameters $\tau_{i,\max}$ for airfoils at the span locations y_i (i=1,2,3,4) are used as design variables. Moreover, the twist angles for airfoils at the span locations y_4 and y_5 are used as design variables. The inboard wing twist variables are fixed to ensure that the main gear strut can be stored inside the wing. The dihedral angles of the four outboard wing sections are also used as design variables. A total of 10 design variables ($\tau_{i,\max}$, twist angles, and dihedral angles) are available to modify the camber surface of a given wing planform. The design vector d_{wing} consists of the 15 planform and camber design variables. With the given fuselage and wing parametric shapes, any new design will have enough volume for 40 passengers and storage of the main gear (see Fig. 1). The passenger cabin model in Fig. 1 uses a seat width of 21 inches, a seat pitch of 48 inches, and an aisle width of 18 inches.
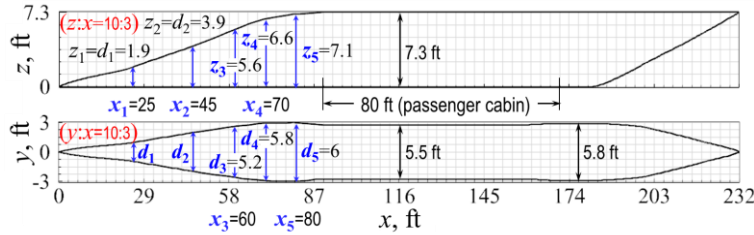
Fig. 2 Fuselage side/top views and design variables.
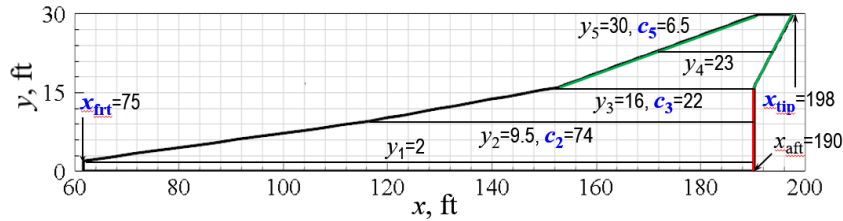
Fig. 3 Wing planform and design variables.

The design vector d_{aft} for aft components has 4 design variables: the longitudinal locations and incident angles for the nacelle and pylon. During the BCO iterations, independent copies $\hat{\theta}_{\text{htail}}$ and $\hat{d}_{\text{aft}}$ of θ_{htail} and d_{aft}, respectively, are used for CFD-based low-boom aft shaping. A parametric Bezier curve with 8 control points is used to define the low-boom target $A_{\text{e,r}}^{\text{target}}$: two control points are used to fix the start and end points of $A_{\text{e,r}}^{\text{target}}$, and the remaining 12 control-point coordinates are used as components of d_{tgt}. The same six auxiliary design variables as in Ref. [41] are the components of d_{LTO} for LTO constraints: trailing edge flap deflection angles for LTO, CG$_x$ offsets for LTO, leading edge flap deflection angle for landing, and main gear length. Flap sizes also affect LTO performance, but they are not used as design variables and change proportionally with wing chords in this paper. The design variables and dimensions of design vectors are listed in Table 3. The independent copy $\hat{D}$ of D is obtained by replacing θ_{htail} and d_{aft} with their independent copies $\hat{\theta}_{\text{htail}}$ and $\hat{d}_{\text{aft}}$, respectively.

Table 3 Design variables and dimensions of design vectors

Symbol	Dimension	Description	Symbol	Dimension	Description
F_{s}	1	Sea-level static thrust	d_{frt}	13	Fuselage front shape parameters
R_{OL}	1	Overland range	d_{wing}	15	Wing shape parameters
H_{OL}	1	Low-boom cruise altitude	D	54	Vector of all design variables
θ_{htail}	1	Horizontal tail deflection angle	$\hat{\theta}_{\text{htail}}$	1	Copy of θ_{htail} for CFD analysis
d_{aft}	4	Aft shape parameters	$\hat{d}_{\text{aft}}$	4	Copy of d_{aft} for CFD analysis
d_{LTO}	6	LTO design parameters	$\hat{D}$	54	Copy of D for CFD analysis
d_{tgt}	12	Shape parameters for target A_{e}			

B. Calibrated Lift Method

It has been demonstrated in Ref. [41] that a feasible low-boom design can be obtained with minor wing modifications of a plausible low-boom design. One major source for discrepancy between these two low-boom designs

is that the root section of the wing inside the fuselage is used for low-fidelity aero analyses, but the wing inside the fuselage is removed to form the watertight geometry for CFD analysis. So, it is natural to remove some of the wing inside the fuselage for more accurate low-fidelity aero analyses. This idea can be implemented by using a truncation parameter y_{rt} (see Fig. 4) for the wing root section. Only the wing geometry from $y = y_{rt}$ to the wing tip is used for low-fidelity aero analyses. The truncated wing is shifted so that the root airfoil is at $y = 0$. This truncated and shifted wing will be referred to as the calibrated wing. The calibrated wing is used to generate the geometry inputs for low-fidelity aero analysis codes. The value of y_{rt} will be determined by the low-fidelity aero analysis code LTSTAR [43] and the CFD analysis: the total wing lift from LTSTAR applied to the calibrated wing equals the total CFD lift for the watertight geometry up to the end of the wing in the effective distance direction (determined by the blue Mach angle cut plane in Fig. 4).
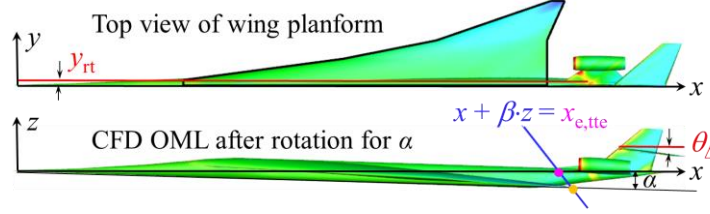
Fig. 4 Illustration of two calibration parameters.

The tail lift is calibrated using a tail rotation angle adjustment parameter θ_Δ (see Fig. 4). This parameter determines the calibrated tail rotation angle ($\theta_{htail} - \theta_\Delta$) for low-fidelity aero analyses of any design with a tail rotation angle of θ_{htail}. The calibrated tail rotation angle makes the total tail lift from LTSTAR equal the total CFD lift after the wing, which includes the lift generated by the pylon and horizontal tail, as well as the interference lift from the nacelle and fuselage.

Figure 4 illustrates the two calibration parameters y_{rt} and θ_Δ. The x-axis is along the flow direction at the start of overland cruise and the fuselage nose is at the origin. The outer mold line (OML) in Fig. 4 is the CFD geometry after the rotation for α. The effective distance location $x_{e,tte}$ (indicated by the pink dot in Fig. 4) is determined by the intersection point of the x-axis and the Mach angle cut plane (shown by the blue line) passing through the trailing edge of the wing tip airfoil (shown by the orange dot in Fig. 4). Note that $x_{e,tte}$ also depends on α.

To make the LTSTAR analysis as accurate as the CFD analysis for the predictions of the wing lift and total lift, the calibration parameters y_{rt} and θ_Δ for a design vector $\boldsymbol{D}$ are the optimal solutions of the following optimization problem.

$$\min_{y_{rt}, \, \theta_\Delta} \left| A_{e,MiFi}^{lift}(x_{e,tte}, \boldsymbol{D}) - A_{e,CFD}^{lift}(x_{e,tte}, \boldsymbol{D}) \right| + \left| A_{e,MiFi}^{lift}(l_e, \boldsymbol{D}) - A_{e,CFD}^{lift}(l_e, \boldsymbol{D}) \right| \tag{3}$$

In Eq. (3), $A_{e,CFD}^{lift}(\boldsymbol{D})$ is computed using M_{OL} and the angle of attack that matches the CFD total lift with the weight of $\boldsymbol{D}$ at the start of overland cruise. The lift equivalent area $A_{e,MiFi}^{lift}(\boldsymbol{D})$ is generated by LTSTAR using the calibrated wing of $\boldsymbol{D}$ and the horizontal tail of $\boldsymbol{D}$ at the calibrated tail rotation angle of ($\theta_{htail} - \theta_\Delta$), where θ_{htail} is the tail rotation angle of $\boldsymbol{D}$ for the CFD analysis. The same M_{OL} and angle of attack for the CFD analysis are used for calculation of $A_{e,MiFi}^{lift}(\boldsymbol{D})$ by LTSATR. Equation (3) has an ideal optimal value of zero.

Once the calibration parameters y_{rt} and θ_Δ are generated by solving Eq. (3), y_{rt} determines the calibrated wing and θ_Δ defines the calibrated tail rotation angle for *all* low-fidelity aero analyses of $\boldsymbol{D}$ in the *entire* flight envelope. This method will be called the calibrated lift method, which leads to many multifidelity models for all mission performance metrics (such as MTOGW and range). The calibrated lift method does not have the fidelity of CFD analysis, but it has higher fidelity than the original low-fidelity aero analyses in the sense that LTSTAR, when applied with the calibrated wing and the calibrated tail rotation angle, reproduces the CFD wing lift and total lift at the start of overland cruise.

The calibrated lift method described above is a multifidelity method because the mission analysis for each $\boldsymbol{D}$ is calibrated/tuned by one CFD solution of $\boldsymbol{D}$. Reference [45] reviews multifidelity methods for uncertainty propagation, inference, and optimization. It categorizes multifidelity methods according to three classes of strategies: adaptation, fusion, and filtering. More specifically, the wing lift and total lift at the start of overland cruise computed using the calibrated lift method with LTSTAR can be considered as tuned low-fidelity models reviewed in Ref. [46].

C. CFD-Based Multiobjective MDO for Low-Boom Supersonic Transports

The following CFD-based multiobjective MDO problem is an improvement of the mixed-fidelity low-boom MDO problem in Ref. [41]. The mission performance metrics in Eq. (4), such as TOGW_{OL}, R_{OL}, $\text{CG}_{x,\text{aft}}$, and $g_i(\boldsymbol{D})$, are computed using the calibrated lift method in Sec. II.B instead of the original low-fidelity aero analyses in Ref. [41]. The objectives are modified to optimize the low-boom mission performance for a fixed cruise Mach, instead of exploring the boundary of the overland cruise Mach and range for low-boom designs with the lowest MTOGW [41].

$$\min_{\boldsymbol{D}} \{\text{TOGW}_{\text{OL}}, -R_{\text{OL}}\}$$
$$\text{subject to } \boldsymbol{l} \leq \boldsymbol{D} \leq \boldsymbol{u}$$
$$g_i(\boldsymbol{D}) \geq 0 \ (1 \leq i \leq 9)$$
$$\text{CG}_{x,\text{aft}} - \text{CP}_{x,\text{CFD}} \geq 1 \tag{4}$$
$$\left\| A_{\text{e,r}}(\boldsymbol{D}) - A_{\text{e,r}}^{\text{target}}(\boldsymbol{D}) \right\|_k \leq \varepsilon$$
$$\text{PLdB}\left(A_{\text{e,r}}^{\text{target}}(\boldsymbol{D})\right) \leq 70$$

The inequalities $g_i(\boldsymbol{D}) \geq 0$ $(1 \leq i \leq 9)$ correspond to the following mission constraints.
   (II.1) Center-of-gravity (CG) margin to prevent tip over on the ground ≥ 4 ft (i.e., the longitudinal CG of the aircraft at empty weight is at least 4 ft before the main gear longitudinal location).
   (II.2) Static margin (SM) for overland cruise $\geq 2\%$ of the mean aerodynamic chord of the wing (MAC).
   (II.3) LTO SMs $\geq 2\%$ of MAC.
   (II.4) Tail rotation angles for trim at LTO $\geq -20°$.
   (II.5) LTO field lengths ≤ 8350 ft.
   (II.6) Approach velocity ≤ 150 kt at altitude of 1000 ft.
   (II.7) $\boldsymbol{D}$ has storage space for main gear and carries 40 passengers for both overland and overwater missions.
   (II.8) $\boldsymbol{D}$ has an overwater mission with cruise Mach of 1.8, range of 3600 nm, and cruise ceiling of 60,000 ft.
   (II.9) $\boldsymbol{D}$ has an overland mission with cruise Mach of M_{OL}, range of R_{OL}, and cruise altitude of H_{OL}.

The objectives in Eq. (4) are for the optimal low-boom mission performance. Note that minimizing MTOGW is mainly to improve the overwater cruise efficiency, when $\text{MTOGW} = \text{TOGW}_{\text{OW}}$ for a much longer overwater range than the overland range. The overwater mission does not have any low-boom requirement and the cruise altitude is determined by the Flight Optimization System (FLOPS) [47] to be optimal for fuel burn. In contrast, the overland cruise efficiency has a low-boom penalty, because the overland cruise flight must be at the specified cruise altitude H_{OL} to satisfy the imposed low-boom constraints for $A_{\text{e,r}}$ in Eq. (4). To attain a low-boom design with the optimal overland cruise efficiency, TOGW_{OL} instead of MTOGW is used as an objective function in Eq. (4).

In Eq. (4), $\boldsymbol{l} \leq \boldsymbol{D} \leq \boldsymbol{u}$ is the standard constraint to define the ranges of design variables. Even though the constraints (II.1)-(II.9) (represented by $g_i(\boldsymbol{D}) \geq 0$) appear to be the same as those in Ref. [41], their calculations use the calibrated lift method in Sec. II.B. See Ref. [41] for a detailed explanation of the constraints (II.1)-(II.9) and why they can be written mathematically as $g_i(\boldsymbol{D}) \geq 0$ $(1 \leq i \leq 9)$. The upper bound for the LTO field lengths is increased from 8300 ft in Ref. [41] to 8350 ft in this paper. This means an insignificant reduction of the margin of 1700 ft for LTO field lengths in Ref. [41] by 50 ft. The constraint $\text{CG}_{x,\text{aft}} - \text{CP}_{x,\text{CFD}} \geq 1$ is for trim at the start of overland cruise with fuel redistribution. The fuel volume is assumed to be the sum of fixed fractions of the longitudinal wing and fuselage volume distributions. This allows defining a preliminary CG_x location vs weight diagram when combined with the component weight and CG_x estimates from FLOPS [47,48]. With enough fuel storage space before the $\text{CP}_{x,\text{CFD}}$ at the start of low-boom cruise for a low-boom supersonic transport, it is easy to shift the fuel CG_x forward for the cruise trim when needed. So, the trim at the start of low-boom cruise (i.e., $\text{CG}_x = \text{CP}_{x,\text{CFD}}$) can be achieved with a redistribution of fuel if $\text{CG}_{x,\text{aft}} - \text{CP}_{x,\text{CFD}} \geq 1$. Here the trim margin of 1 ft is empirical. The constraints for $A_{\text{e,r}}$ in Eq. (4) define a feasible low-boom design with PLdB ≤ 70.

D. Multifidelity Models for Low-Boom MDO

Note that the calibrated lift method in Sec. II.B requires one CFD solution for the mission analysis of each design. So, Eq. (4) is a CFD-based multiobjective MDO problem. To save the computational cost, multifidelity models for all $\boldsymbol{D}$ based on one CFD solution will be used to solve Eq. (4).

The multifidelity models for solving Eq. (4) are defined by any given feasible low-boom design and are updated when another feasible low-boom design is generated in the MDO iteration process. For a given feasible low-boom design $\hat{\boldsymbol{D}}_{\text{aft}}$, let $\hat{y}_{\text{rt}}$ and $\hat{\theta}_{\Delta}$ be determined by solving Eq. (3) for $\boldsymbol{D} = \hat{\boldsymbol{D}}_{\text{aft}}$. In this case, $A_{\text{e,CFD}}^{\text{lift}}(\hat{\boldsymbol{D}}_{\text{aft}})$ and $A_{\text{e,MiFi}}^{\text{lift}}(\hat{\boldsymbol{D}}_{\text{aft}})$ are computed using CFD and LTSATR, respectively, for M_{OL} and the CFD angle of attack. Then the mission performance metrics are computed using the low-fidelity aero analysis codes applied on the calibrated wing for the truncation

parameter $\hat{y}_{\mathrm{rt}}$ and the horizontal tail at the calibrated tail rotation angle ($\theta_{\mathrm{htail}}-\hat{\theta}_{\Delta}$) for any design vector $\boldsymbol{D}$. These mission performance metrics are used as the multifidelity models for the calibrated mission performance metrics in Eq. (4). The multifidelity approximation here is to use one CFD solution for the calibrated low-fidelity aero analyses of all design vectors instead of one design vector.

For multifidelity A_{e} models, $A_{\mathrm{e,MiFi}}^{\mathrm{lift}}(\boldsymbol{D})$ provides the initial approximation of $A_{\mathrm{e,CFD}}^{\mathrm{lift}}(\boldsymbol{D})$ for any design vector $\boldsymbol{D}$. Here $A_{\mathrm{e,MiFi}}^{\mathrm{lift}}(\boldsymbol{D})$ is computed by applying LTSTAR on the calibrated wing of $\boldsymbol{D}$ for the truncation parameter $\hat{y}_{\mathrm{rt}}$ and the horizontal tail of $\boldsymbol{D}$ at the calibrated tail rotation angle of ($\theta_{\mathrm{htail}}-\hat{\theta}_{\Delta}$), while the total lift generated by LTSTAR matches the weight of $\boldsymbol{D}$ at the start of overland cruise. The multifidelity models for $A_{\mathrm{e,CFD}}^{\mathrm{lift}}$ and $A_{\mathrm{e,r}}$ require the following two correction terms.

$$\Delta A_{\mathrm{e,CFD}}^{\mathrm{lift}}\left(x_{\mathrm{e}}, \widehat{\boldsymbol{D}}_{\mathrm{aft}}\right) = A_{\mathrm{e,CFD}}^{\mathrm{lift}}\left(x_{\mathrm{e}}, \widehat{\boldsymbol{D}}_{\mathrm{aft}}\right) - A_{\mathrm{e,MiFi}}^{\mathrm{lift}}\left(x_{\mathrm{e}}, \widehat{\boldsymbol{D}}_{\mathrm{aft}}\right) \qquad \text{(Lift } A_{\mathrm{e}} \text{ correction term)} \qquad (5\mathrm{a})$$

$$\Delta A_{\mathrm{e,r}}\left(x_{\mathrm{e}}, \widehat{\boldsymbol{D}}_{\mathrm{aft}}\right) = A_{\mathrm{e,r}}\left(x_{\mathrm{e}}, \widehat{\boldsymbol{D}}_{\mathrm{aft}}\right) - A_{\mathrm{e,LoFi}}^{\mathrm{volume}}\left(x_{\mathrm{e}}, \widehat{\boldsymbol{D}}_{\mathrm{aft}}\right) - A_{\mathrm{e,CFD}}^{\mathrm{lift}}\left(x_{\mathrm{e}}, \widehat{\boldsymbol{D}}_{\mathrm{aft}}\right) \quad \text{(Total } A_{\mathrm{e}} \text{ correction term)} \quad (5\mathrm{b})$$
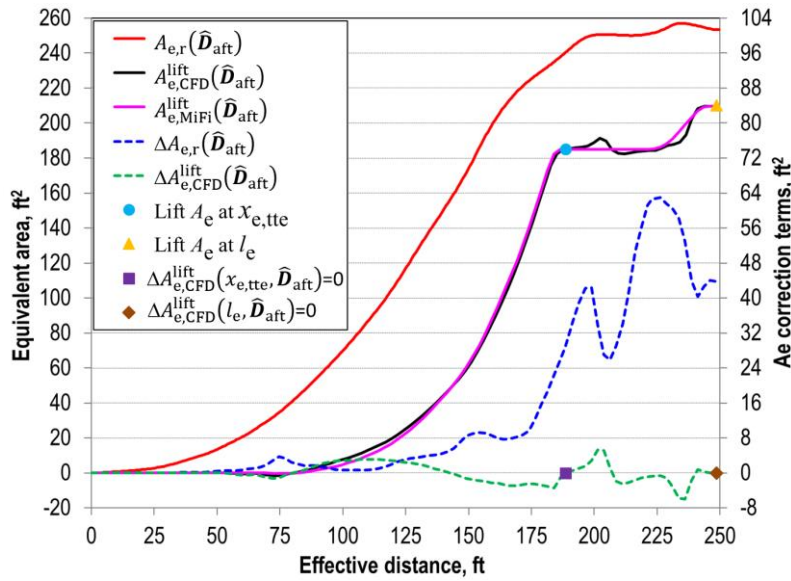
Fig. 5 Equivalent areas and A_{e} correction terms from A_{e} calibration analysis.

Figure 5 shows $A_{\mathrm{e,r}}(\widehat{\boldsymbol{D}}_{\mathrm{aft}})$, $A_{\mathrm{e,CFD}}^{\mathrm{lift}}(\widehat{\boldsymbol{D}}_{\mathrm{aft}})$, $A_{\mathrm{e,MiFi}}^{\mathrm{lift}}(\widehat{\boldsymbol{D}}_{\mathrm{aft}})$ defined by the optimal solution ($\hat{y}_{\mathrm{rt}}$, $\hat{\theta}_{\Delta}$) of Eq. (3) with $\boldsymbol{D} = \widehat{\boldsymbol{D}}_{\mathrm{aft}}$, and the A_{e} correction terms defined by Eqs. (5a-5b). The secondary vertical axis in Fig. 5 is used for a better view of the correction terms. The data in Fig. 5 are generated by the last BCO iteration cycle for the design study in Sec. III. The corresponding calibration parameters $\hat{y}_{\mathrm{rt}}$ and $\hat{\theta}_{\Delta}$ are 1.270 ft and 3.803°, respectively.

Note that $\Delta A_{\mathrm{e,CFD}}^{\mathrm{lift}}(x_{\mathrm{e,tte}}, \widehat{\boldsymbol{D}}_{\mathrm{aft}}) = \Delta A_{\mathrm{e,CFD}}^{\mathrm{lift}}(l_{\mathrm{e}}, \widehat{\boldsymbol{D}}_{\mathrm{aft}}) = 0$ because the optimal objective of Eq. (3) is zero. So, adding any multiple of $\Delta A_{\mathrm{e,CFD}}^{\mathrm{lift}}(\widehat{\boldsymbol{D}}_{\mathrm{aft}})$ in the interval $[0, x_{\mathrm{e,tte}}]$ does not change the total lift on the wing and adding any multiple of $\Delta A_{\mathrm{e,CFD}}^{\mathrm{lift}}(\widehat{\boldsymbol{D}}_{\mathrm{aft}})$ in the interval $[x_{\mathrm{e,tte}}, l_{\mathrm{e}}]$ does not change the total aft lift after the wing. An accurate prediction of $A_{\mathrm{e,CFD}}^{\mathrm{lift}}(\boldsymbol{D})$ can be obtained by a linear combination of $A_{\mathrm{e,MiFi}}^{\mathrm{lift}}(\boldsymbol{D})$ and $\Delta A_{\mathrm{e,CFD}}^{\mathrm{lift}}(\widehat{\boldsymbol{D}}_{\mathrm{aft}})$, then $\Delta A_{\mathrm{e,r}}(\widehat{\boldsymbol{D}}_{\mathrm{aft}})$ can be used to recover $A_{\mathrm{e,r}}(\boldsymbol{D})$. The multifidelity A_{e} models $A_{\mathrm{e,MuFi}}^{\mathrm{lift}}$ and $A_{\mathrm{e,MuFi}}$ are defined as follows.

$$A_{\mathrm{e,MuFi}}^{\mathrm{lift}}(x_{\mathrm{e}}, \boldsymbol{D}) = A_{\mathrm{e,MiFi}}^{\mathrm{lift}}(x_{\mathrm{e}}, \boldsymbol{D}) + \frac{A_{\mathrm{e,MiFi}}^{\mathrm{lift}}(x_{\mathrm{e,tte}}, \boldsymbol{D})}{A_{\mathrm{e,CFD}}^{\mathrm{lift}}(x_{\mathrm{e,tte}}(\widehat{\boldsymbol{D}}_{\mathrm{aft}}), \widehat{\boldsymbol{D}}_{\mathrm{aft}})} \cdot \Delta A_{\mathrm{e,CFD}}^{\mathrm{lift}}(\hat{x}_{\mathrm{e}}, \widehat{\boldsymbol{D}}_{\mathrm{aft}})$$

$$\text{for } 0 \leq x_{\mathrm{e}} \leq x_{\mathrm{e,tte}} \qquad \text{(Multifidelity front lift equivalent area)} \tag{6a}$$

$$A_{\mathrm{e,MuFi}}^{\mathrm{lift}}(x_{\mathrm{e}}, \boldsymbol{D}) = A_{\mathrm{e,MiFi}}^{\mathrm{lift}}(x_{\mathrm{e}}, \boldsymbol{D}) + \frac{A_{\mathrm{e,MiFi}}^{\mathrm{lift}}(l_{\mathrm{e}}, \boldsymbol{D}) - A_{\mathrm{e,MiFi}}^{\mathrm{lift}}(x_{\mathrm{e,tte}}, \boldsymbol{D})}{A_{\mathrm{e,CFD}}^{\mathrm{lift}}(l_{\mathrm{e}}(\widehat{\boldsymbol{D}}_{\mathrm{aft}}), \widehat{\boldsymbol{D}}_{\mathrm{aft}}) - A_{\mathrm{e,CFD}}^{\mathrm{lift}}(x_{\mathrm{e,tte}}(\widehat{\boldsymbol{D}}_{\mathrm{aft}}), \widehat{\boldsymbol{D}}_{\mathrm{aft}})} \cdot \Delta A_{\mathrm{e,CFD}}^{\mathrm{lift}}(\hat{x}_{\mathrm{e}}, \widehat{\boldsymbol{D}}_{\mathrm{aft}})$$

$$\text{for } x_{\mathrm{e,tte}} \leq x_{\mathrm{e}} \leq l_{\mathrm{e}} \qquad \text{(Multifidelity aft lift equivalent area)} \tag{6b}$$

$$A_{e,\text{MuFi}}(x_e, \boldsymbol{D}) = A_{e,\text{MuFi}}^{\text{lift}}(x_e, \boldsymbol{D}) + A_{e,\text{LoFi}}^{\text{volume}}(x_e, \boldsymbol{D}) + \frac{A_{e,\text{MuFi}}^{\text{lift}}(l_e, \boldsymbol{D})}{A_{e,\text{CFD}}^{\text{lift}}(l_e(\widehat{\boldsymbol{D}}_{\text{aft}}), \widehat{\boldsymbol{D}}_{\text{aft}})} \cdot \Delta A_{e,r}(\hat{x}_e, \widehat{\boldsymbol{D}}_{\text{aft}}) \tag{6c}$$

$$\text{for } 0 \le x_e \le l_e \qquad \text{(Multifidelity total equivalent area)}$$

Here the modified effective distance $\hat{x}_e$ is computed by aligning the corresponding effective distance locations of wings and tails of $\widehat{\boldsymbol{D}}_{\text{aft}}$ and $\boldsymbol{D}$ (illustrated by the blue and black dots in Fig. 6, where x-axis is along the flow direction).

$$\hat{x}_e = \frac{x_{e,\text{rle}}(\widehat{\boldsymbol{D}}_{\text{aft}})}{x_{e,\text{rle}}} \cdot x_e \qquad\qquad \text{for } 0 \le x_e \le x_{e,\text{rle}} \tag{7a}$$
$$\text{(ahead of wing)}$$

$$\hat{x}_e = x_{e,\text{rle}}(\widehat{\boldsymbol{D}}_{\text{aft}}) + \frac{x_{e,\text{tte}}(\widehat{\boldsymbol{D}}_{\text{aft}}) - x_{e,\text{rle}}(\widehat{\boldsymbol{D}}_{\text{aft}})}{x_{e,\text{tte}} - x_{e,\text{rle}}} \cdot (x_e - x_{e,\text{rle}}) \qquad \text{for } x_{e,\text{rle}} \le x_e \le x_{e,\text{tte}} \tag{7b}$$
$$\text{(wing segment)}$$

$$\hat{x}_e = x_{e,\text{tte}}(\widehat{\boldsymbol{D}}_{\text{aft}}) + \frac{x_{e,\text{frt}}(\widehat{\boldsymbol{D}}_{\text{aft}}) - x_{e,\text{tte}}(\widehat{\boldsymbol{D}}_{\text{aft}})}{x_{e,\text{frt}} - x_{e,\text{tte}}} \cdot (x_e - x_{e,\text{tte}}) \qquad \text{for } x_{e,\text{tte}} \le x_e \le x_{e,\text{frt}} \tag{7c}$$
$$\text{(between wing and horizontall tail)}$$

$$\hat{x}_e = x_{e,\text{frt}}(\widehat{\boldsymbol{D}}_{\text{aft}}) + \frac{x_{e,\text{aft}}(\widehat{\boldsymbol{D}}_{\text{aft}}) - x_{e,\text{frt}}(\widehat{\boldsymbol{D}}_{\text{aft}})}{x_{e,\text{aft}} - x_{e,\text{frt}}} \cdot (x_e - x_{e,\text{frt}}) \qquad \text{for } x_{e,\text{frt}} \le x_e \le x_{e,\text{aft}} = l_e \tag{7d}$$
$$\text{(horizontall tail segment)}$$
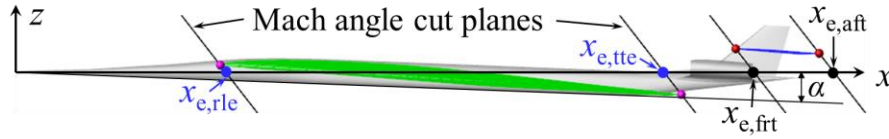
Fig. 6 Effective distance locations for wing and horizontal tail.

Equations (7a-7d) ensure that the lift A_e corrections in Eqs. (6a-6b) are performed for the corresponding x_e locations of the wings and horizontal tails of $\boldsymbol{D}$ and $\widehat{\boldsymbol{D}}_{\text{aft}}$. For example, the lift A_e correction for the wing of $\boldsymbol{D}$ starts and ends over the effective distance range of the wing of $\boldsymbol{D}$ using the correction term value over the corresponding effective distance range of the wing of $\widehat{\boldsymbol{D}}_{\text{aft}}$. The scaling factors in Eqs. (6a-6b) make the lift A_e correction magnitudes proportional to the lifts generated by the wing and horizontal tail of $\boldsymbol{D}$, respectively. The scaling factor in Eq. (6c) makes the correction magnitude proportional to the changes of the cruise weight and altitude. One could verify that $A_{e,\text{MuFi}}^{\text{lift}}(\widehat{\boldsymbol{D}}_{\text{aft}}) = A_{e,\text{CFD}}^{\text{lift}}(\widehat{\boldsymbol{D}}_{\text{aft}})$ and $A_{e,\text{MuFi}}^{\text{lift}}(\widehat{\boldsymbol{D}}_{\text{aft}}) = A_{e,r}(\widehat{\boldsymbol{D}}_{\text{aft}})$ using Eqs. (6a-6c). That is, the multifidelity A_e models in Eqs. (6a-6c) recover the $A_{e,\text{CFD}}^{\text{lift}}$ and $A_{e,r}$ of $\widehat{\boldsymbol{D}}_{\text{aft}}$.

Note that the multifidelity models depend on the feasible low-boom design $\widehat{\boldsymbol{D}}_{\text{aft}}$ and the next feasible low-boom design for updating the multifidelity models will be generated by the refined BCO method using the current multifidelity models. The choice of using one feasible low-boom design $\widehat{\boldsymbol{D}}_{\text{aft}}$ (instead of any design) for the calibrated lift analyses of all designs is empirical and its validity is confirmed by the design study in Sec. III.

The multifidelity A_e models in Eqs. (6a-6c) use both additive and multiplicative correction terms for design variables in $\boldsymbol{D}$, which could be considered as multifidelity adaptation methods [45]. Moreover, these multifidelity models are functions of x_e and a piecewise linear transformation of x_e is defined by Eqs. (7a-7d) to align the correction terms with the low-fidelity equivalent areas. The multifidelity models in Eqs. (6a-6c) are not about predicting a finite number of high-fidelity metrics (such as the CFD lift and drag coefficients). They are used to predict the high-fidelity distribution functions $A_{e,\text{CFD}}(x_e, \boldsymbol{D})$ and $A_{e,r}(x_e, \boldsymbol{D})$. In the literature, approximations of high-fidelity distribution functions are typically based on reduced order models. Reference [49] includes an example of using a reduced order model to approximate the CFD surface pressure distribution in airfoil inverse design optimization.

The multifidelity models for the mission performance metrics and equivalent areas achieve two goals: 1) better predictions of the CFD wing lift and total lift at the start of overland cruise and 2) accurate predictions of $A_{e,\text{CFD}}^{\text{lift}}$ and $A_{e,r}$ over the entire effective distance interval $[0, l_e]$. These multifidelity models aim to achieve the high-fidelity accuracies of lift related metrics or functions that are relevant to the sonic boom analysis.

E. Refined BCO Method

The inverse design constraint makes the multiobjective MDO [Eq. (4)] difficult to solve as a numerical optimization problem (see sec. II.A in Ref. [41] for a detailed explanation). The BCO method in Ref. [41] is refined with a better trade method for the maximum overland range and the multifidelity models in Sec. II.D for higher fidelity solutions of low-boom MDO. The following optimization subproblems for the refined BCO method use the mission performance metrics generated by the multifidelity models for aero data and the low-boom inverse design objective based on the multifidelity A_e models. Equations (8a-8f) implicitly depend on $\hat{y}_{rt}$ and $\hat{\theta}_A$. The motivation of decoupling the CFD-based multiobjective low-boom MDO problem [Eq. (4)] into weakly coupled optimization subproblems was discussed in Ref. [41]. The main reason is that no existing numerical algorithm is capable of solving Eq. (4).

$$\min_{\boldsymbol{d}_{tgt}} \mathrm{PLdB}\left(A_{e,r,0}^{target}\right) \text{ subject to } A_{e,r,0}^{target}\left(\tfrac{l_{e,0}}{2}\right)/A_{e,r,0}^{target}(l_{e,0}) \geq \delta, \ A_{e,r,0}^{target}(l_{e,0})/A_{MuFi}^{lift}(l_{e,0}, \boldsymbol{D}_0) = \mu \tag{8a}$$
$$\text{(Baseline low-boom target optimization)}$$

$$\min_{\boldsymbol{d}_{frt},\boldsymbol{d}_{wing},\boldsymbol{\theta}_{htail}} \left\{ \mathrm{TOGW}_{OL}, \left\|A_{e,MuFi}(\boldsymbol{D}){-}A_{e,r}^{target}(\boldsymbol{D})\right\|_{k,\lambda} \right\} \text{ subject to } \boldsymbol{l} \leq \boldsymbol{D} \leq \boldsymbol{u}, \ g_i(\boldsymbol{D}) \geq 0 \ (7 \leq i \leq 9) \tag{8b}$$
$$\text{(Low-boom MDO using multifidelity models)}$$

$$\max_{R_{OL},H_{OL}} R_{OL} \text{ subject to } g_8(\boldsymbol{D}) \geq 0, \ g_9(\boldsymbol{D}) \geq 0, \mathrm{PLdB}\left(A_{e,r}^{target}(\boldsymbol{D})\right) \leq 70, \ \alpha = \alpha_{LoW} \tag{8c}$$
$$\text{(Range maximization for overland mission)}$$

$$\min_{F_s,\boldsymbol{d}_{LTO}} \mathrm{TOGW}_{OL} \text{ subject to } \boldsymbol{l} \leq \boldsymbol{D} \leq \boldsymbol{u}, \ g_i(\boldsymbol{D}) \geq 0 \ (1 \leq i \leq 9) \tag{8d}$$
$$\text{(Engine thrust and mission constraint optimization)}$$

$$\min_{\hat{\theta}_{htail}} \left|A_{e,CFD}\left(l_e, \widehat{\boldsymbol{D}}\right) - A_{e,MuFi}^{lift}(l_e, \boldsymbol{D})\right| \text{ subject to } \boldsymbol{l} \leq \widehat{\boldsymbol{D}} \leq \boldsymbol{u}, \ \widehat{\boldsymbol{d}}_{aft} = \boldsymbol{d}_{aft} \tag{8e}$$
$$\text{(Adjustment of CFD tail rotation angle for lift matching)}$$

$$\min_{\hat{\theta}_{htail},\widehat{\boldsymbol{d}}_{aft}} \left\|A_{e,r}\left(\widehat{\boldsymbol{D}}\right) - A_{e,r}^{target}(\boldsymbol{D})\right\|_k \text{ subject to } \boldsymbol{l} \leq \widehat{\boldsymbol{D}} \leq \boldsymbol{u} \tag{8f}$$
$$\text{(CFD-based low-boom aft shaping of MDO solution)}$$

The low-boom target $A_{e,r}^{target}(\boldsymbol{D})$ in the above formulations is defined by the following scaling formula.

$$A_{e,r}^{target}(x_e, \boldsymbol{D}) = \frac{A_{e,MuFi}^{lift}(l_e,\boldsymbol{D})}{A_{e,MuFi}^{lift}(l_{e,0},\boldsymbol{D}_0)} \cdot A_{e,r,0}^{target}\left(\frac{l_{e,0}}{l_e} \cdot x_e\right) \text{ for Eqs. (8b), (8c), and (8f)} \tag{9}$$

Equation (9) is the same as the weight scaling formula [eq. (3a)] in Ref. [41] if $\boldsymbol{D}_0$ and $\boldsymbol{D}$ have the same overland cruise altitude. The relationship between $A_{e,MuFi}^{lift}(l_e)$ and W_{crs} can be formulated as the following equation.

$$A_{e,MuFi}^{lift}(l_e) = A_{e,MuFi}^{lift}(l_e) + A_{e,LoFi}^{volume}(l_e) = A_{e,m}(l_e) = \frac{\beta}{\rho_\infty \cdot U_\infty^2} \cdot W_{crs} \tag{10}$$

The first equality in Eq. (10) follows from $A_{e,LoFi}^{volume}(l_e) = 0$, the second equality is the definition for $A_{e,m}(l_e)$, and the third equality is the relationship between $A_{e,m}(l_e)$ and W_{crs} [8] {e.g., see eq. (6) in Ref. [15]}. So, the scaling in Eq. (9) is proportional to W_{crs} and inversely proportional to the ambient density ρ_∞ at H_{OL}.

The optimization problems defined by Eqs. (8a-8f) are just iteration steps to get a solution of Eq. (4) and they do not include some of the actual design requirements in Eq. (4). The following post-optimization conditions must be satisfied by a solution pair $(\boldsymbol{D}, \widehat{\boldsymbol{D}})$ of Eqs. (8a-8f) to obtain a solution of Eq. (4).

$$\left\|A_{e,MuFi}(\boldsymbol{D}){-}A_{e,r}^{target}(\boldsymbol{D})\right\|_{k,\lambda} \leq \varepsilon \tag{11a}$$

$$\left\|A_{e,r}\left(\widehat{\boldsymbol{D}}\right) - A_{e,r}^{target}(\boldsymbol{D})\right\|_k \leq \varepsilon \tag{11b}$$

$$\mathrm{CG}_{x,aft} - \mathrm{CP}_{x,CFD} \geq 1 \tag{11c}$$

Equations (11a-11b) are the implicit requirements for inverse design optimization problems [Eqs. (8b) and (8f)], respectively. Equation (11c) is the CFD trim constraint in Eq. (4), which can only be checked after the optimal solution of Eq. (8e) or (8f) is obtained. If $\widehat{D} \approx D$ (which is the convergence criterion of the refined BCO method), D is an optimal solution for each of Eqs. (8b-8d), $\widehat{D}$ is an optimal solution of Eq. (8e), and Eqs. (11a-11c) hold, then D satisfies all the constraints in Eq. (4). The optimality of D for Eq. (4) is empirically inferred by the optimality of D for Eqs. (8b-8c) without a mathematical proof.

The refined BCO method is represented by the flowchart in Fig. 7. Each optimization problem in Eqs. (8a-8f) is one iteration step of the refined BCO method with Eqs. (11a-11c) as the post-optimization constraints for the BCO iterations. The design vector D and its independent copy $\widehat{D}$ are partitioned into six blocks of design variables: d_{tgt}, $(d_{\mathrm{frt}}, d_{\mathrm{wing}}, \theta_{\mathrm{htail}})$, $(R_{\mathrm{OL}}, H_{\mathrm{OL}})$, $(F_{\mathrm{s}}, d_{\mathrm{LTO}})$, $\widehat{\theta}_{\mathrm{htail}}$, and $(\widehat{\theta}_{\mathrm{htail}}, \widehat{d}_{\mathrm{aft}})$, which are different from the block partitions in Ref. [41]. Each of Eqs. (8a-8f) uses one block of design variables. In the BCO iterations, each optimal solution is used as the initial design for the next optimization problem.
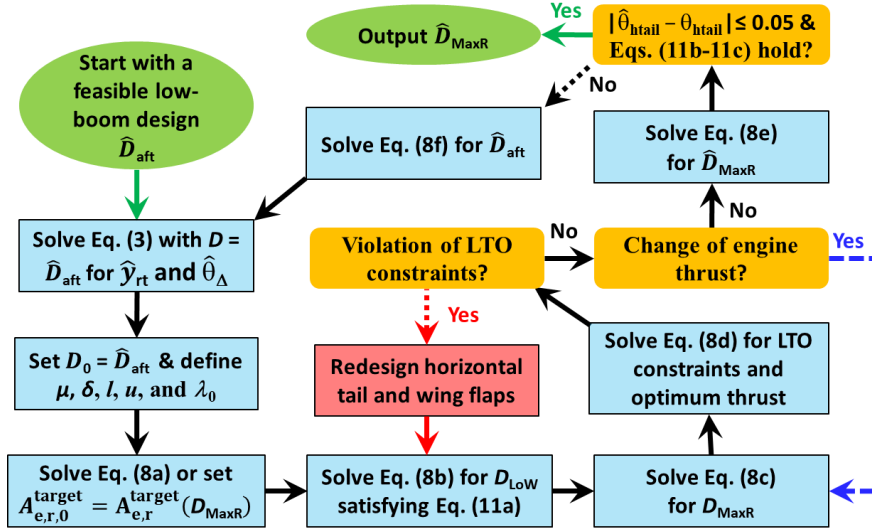
Fig. 7 BCO for low-boom MDO using multifidelity models.

The refined BCO method in Fig. 7 starts with a feasible low-boom design $\widehat{D}_{\mathrm{aft}}$ and solves Eq. (3) with $D = \widehat{D}_{\mathrm{aft}}$ for the calibration parameters $\widehat{y}_{\mathrm{rt}}$ and $\widehat{\theta}_\Delta$. The required feasible low-boom design $\widehat{D}_{\mathrm{aft}}$ could be generated by the BCO method in Ref. [41] or by solving Eq. (8f) first. The calibration parameters $\widehat{y}_{\mathrm{rt}}$ and $\widehat{\theta}_\Delta$ define the multifidelity models for the mission performance metrics and the multifidelity equivalent areas in Eqs. (8a-8e) (see Sec. II.D). The four parameters μ, δ, l, and u are not design variables, but their values have a significant influence on the solution pair of Eqs. (8a-8f). The parameter μ determines how the baseline low-boom target should be defined a priori for low-boom MDO. The difference $\mu - A_{\mathrm{e,r}}(l_{\mathrm{e}}, \widehat{D}_{\mathrm{aft}})/A_{\mathrm{e,CFD}}(l_{\mathrm{e}}, \widehat{D}_{\mathrm{aft}})$ determines proportionally how much $A_{\mathrm{e,r}}(l_{\mathrm{e}}, \widehat{D})$ will deviate above or below $A_{\mathrm{e,r}}^{\mathrm{target}}(l_{\mathrm{e}}, D)$ for the solution $\widehat{D}$ of Eq. (8f). The parameter δ implicitly enforces the CFD trim constraint [Eq. (11c)]. The initial choice of δ is always zero. Once a solution of Eq. (11b) violates Eq. (11c), δ must be set at a value greater than the current value of $A_{\mathrm{e,r}}^{\mathrm{target}}(l_{\mathrm{e}}/2)/A_{\mathrm{e,r}}^{\mathrm{target}}(l_{\mathrm{e}})$. The value of $A_{\mathrm{e,r}}^{\mathrm{target}}(l_{\mathrm{e}}/2)/A_{\mathrm{e,r}}^{\mathrm{target}}(l_{\mathrm{e}})$ will be called the *trim ratio* for any $A_{\mathrm{e,r}}$ target, which is fixed during each iteration cycle of solving Eqs. (8b-8f) [see Eq. (9)]. A target $A_{\mathrm{e,r}}^{\mathrm{target}}$ with a higher trim ratio tends to move $\mathrm{CP}_{x,\mathrm{CFD}}$ of the corresponding feasible low-boom design forward. So, with a proper trim ratio for $A_{\mathrm{e,r}}^{\mathrm{target}}$, the corresponding feasible low-boom design will satisfy Eq. (11c) (see Sec. III). The design vector bounds l and u are extensively discussed in Ref. [40]. The key idea is to avoid having an optimized geometry design variable close to one of its bounds, while using small design ranges so that Eq. (8b) can be solved effectively. In practice, a trial and error approach is required to get a set of appropriate values for δ, l, and u. The fifth parameter λ_0 is usually the x_{e} location of the highest point on $A_{\mathrm{e,LoFi}}(D_0)$. However, as $A_{\mathrm{e,MuFi}}$ becomes very accurate in predicting $A_{\mathrm{e,r}}$, reset $\lambda_0 = l_{\mathrm{e},0}$ for a better aft matching between $A_{\mathrm{e,MuFi}}$ and $A_{\mathrm{e,r}}^{\mathrm{target}}$.

The baseline low-boom target optimization [Eq. (8a)] is solved only when μ or δ is changed. Otherwise, the baseline low-boom target is reset to $A_{\mathrm{e,r}}^{\mathrm{target}}(D_{\mathrm{MaxR}})$. The Pareto frontier of the multiobjective optimization problem [Eq. (8b)] usually requires a significant amount (1-2 days using about 15 parallel design evaluations) of wall-clock time to

generate. The selected solution $\boldsymbol{D}_{\text{Low}}$ of Eq. (8b) is the lowest weight solution on the Pareto frontier that also satisfies Eq. (11a).

The overland range optimization [Eq. (8c)] is completely different from that in Ref. [41]. Because the PLdB requirement is removed from the post-optimization constraint Eq. (11a), PLdB($A_{\text{e,r}}^{\text{target}}(\boldsymbol{D}_{\text{Low}})$) could be greater than 70. For the previous two BCO methods [40,41], this would be considered as a failed attempt to find a low-boom concept due to the infeasible overland mission requirement. For the refined BCO method, this becomes the opportunity to discover the appropriate overland mission requirement. The goal of Eq. (8c) is to get a plausible low-boom design with 70 PLdB when $\boldsymbol{D}_{\text{Low}}$ satisfies Eq. (11a).

To verify that the maximum range solution $\boldsymbol{D}_{\text{MaxR}}$ of Eq. (8c) is always a plausible low-boom design with 70 PLdB, the following equalities will be proved for any design vector $\boldsymbol{D}$ in Eq. (8c) satisfying $\alpha = \alpha_{\text{Low}}$.

$$C_{\text{L}}(\boldsymbol{D}_{\text{Low}}) \cdot S_{\text{ref}}(\boldsymbol{D}_{\text{Low}}) = \frac{2}{\rho_\infty \cdot U_\infty^2} \cdot W_{\text{crs}} \tag{12a}$$

$$A_{\text{e,r}}^{\text{target}}(\boldsymbol{D}) = A_{\text{e,r}}^{\text{target}}(\boldsymbol{D}_{\text{Low}}), A_{\text{e,MuFi}}(\boldsymbol{D}) = A_{\text{e,MuFi}}(\boldsymbol{D}_{\text{Low}}) \tag{12b}$$

In Eq. (12a), W_{crs} and ρ_∞ are the weight at the start of overland cruise and the ambient density at the cruise altitude of $\boldsymbol{D}$, respectively.

Note that Eq. (12a) is the standard lift equation when W_{crs} and ρ_∞ are the cruise weight and the ambient density for $\boldsymbol{D}_{\text{Low}}$, respectively. Because each optimization starts with the optimal solution from the previous optimization subproblem, any design vector $\boldsymbol{D}$ in Eq. (8c) has the same OML as $\boldsymbol{D}_{\text{Low}}$. So, $\boldsymbol{D}$ and $\boldsymbol{D}_{\text{Low}}$ have the same wing reference area. The constraint $\alpha = \alpha_{\text{Low}}$ implies that $\boldsymbol{D}$ has the same lift coefficient as $\boldsymbol{D}_{\text{Low}}$. As a result, Eq. (12a) is also the lift equation for any $\boldsymbol{D}$ in Eq. (8c) satisfying $\alpha = \alpha_{\text{Low}}$. This completes the proof of Eq. (12a).

Because the left side of Eq. (12a) is fixed, the right side of Eq. (12a) is the same for all $\boldsymbol{D}$ satisfying $\alpha = \alpha_{\text{Low}}$. It follows from Eqs. (9), (10), and (12a) that $A_{\text{e,r}}^{\text{target}}(\boldsymbol{D}) = A_{\text{e,r}}^{\text{target}}(\boldsymbol{D}_{\text{Low}})$. Because $\boldsymbol{D}$ and $\boldsymbol{D}_{\text{Low}}$ have the same OML and the same angle of attack, 1) the calibrated lift method yields $A_{\text{e,MiFi}}^{\text{lift}}(x_e, \boldsymbol{D}) = A_{\text{e,MiFi}}^{\text{lift}}(x_e, \boldsymbol{D}_{\text{Low}})$, and 2) $A_{\text{e,LoFi}}^{\text{volume}}(x_e, \boldsymbol{D}) = A_{\text{e,LoFi}}^{\text{volume}}(x_e, \boldsymbol{D}_{\text{Low}})$. The multifidelity total equivalent area $A_{\text{e,MuFi}}$ is uniquely determined by $A_{\text{e,MiFi}}^{\text{lift}}(x_e)$, $A_{\text{e,LoFi}}^{\text{volume}}(x_e)$, the OML, the angle of attack, and the cruise Mach [see Eqs. (6a-6c)]. So, $A_{\text{e,MuFi}}(\boldsymbol{D}) = A_{\text{e,MuFi}}(\boldsymbol{D}_{\text{Low}})$. This completes the proof of Eq. (12b).

An important relationship between PLdB and H_{OL} is that, for a fixed M_{OL} and a fixed $A_{\text{e,r}}^{\text{target}}$, PLdB($A_{\text{e,r}}^{\text{target}}$) is a strictly decreasing function of H_{OL}. That is, the PLdB value of the signature of $A_{\text{e,r}}^{\text{target}}$ propagated from H_{OL} to the ground is a strictly decreasing function of H_{OL}. This relationship has no mathematical proof, but it has been verified for $A_{\text{e,r}}^{\text{target}}$ used in this paper. This relationship allows Eq. (8c) to enforce PLdB($A_{\text{e,r}}^{\text{target}}(\boldsymbol{D})$) = 70 using R_{OL} and H_{OL}.

If PLdB($A_{\text{e,r}}^{\text{target}}(\boldsymbol{D}_{\text{Low}})$) > 70, let $\boldsymbol{D}$ be any design obtained by reducing the overland range of $\boldsymbol{D}_{\text{Low}}$. The reduced range decreases the cruise weight W_{crs} of $\boldsymbol{D}$, which implies that the angle of attack α for $\boldsymbol{D}$ is smaller than α_{Low} at the cruise altitude of $\boldsymbol{D}_{\text{Low}}$. If the overland cruise altitude of $\boldsymbol{D}$ increases and the cruise weight of $\boldsymbol{D}$ does not change, the reduced air density at the increased altitude requires a higher lift coefficient to match the same cruise weight, which means that α for $\boldsymbol{D}$ increases. Even though the cruise weight actually changes with the cruise altitude, the effect of the cruise weight change on the required lift coefficient is eclipsed by the air density change. As a result, α for $\boldsymbol{D}$ increases if the overland cruise altitude of $\boldsymbol{D}$ increases. There exists an increased altitude for $\boldsymbol{D}$ such that $\alpha = \alpha_{\text{Low}}$. Because $\boldsymbol{D}_{\text{Low}}$ satisfies Eq. (11a), Eq. (12b) implies that $\boldsymbol{D}$ is a plausible low-boom design and $A_{\text{e,r}}^{\text{target}}(\boldsymbol{D}) = A_{\text{e,r}}^{\text{target}}(\boldsymbol{D}_{\text{Low}})$. Because $\boldsymbol{D}$ has a higher cruise altitude than $\boldsymbol{D}_{\text{Low}}$, PLdB($A_{\text{e,r}}^{\text{target}}(\boldsymbol{D})$) < PLdB($A_{\text{e,r}}^{\text{target}}(\boldsymbol{D}_{\text{Low}})$) follows from the relationship between PLdB and H_{OL} mentioned above. With an appropriate value of R_{OL}, there exists an increased altitude H_{OL} for $\boldsymbol{D}$ such that $\boldsymbol{D}$ is a plausible low-boom design with PLdB($A_{\text{e,r}}^{\text{target}}(\boldsymbol{D})$) = 70. That is, the solution $\boldsymbol{D}_{\text{Low}}$ of Eqs. (8b) and (11a) can always be converted into a plausible low-boom design $\boldsymbol{D}_{\text{MaxR}}$ with 70 PLdB. The cost is a reduced overland range for $\boldsymbol{D}_{\text{MaxR}}$ when PLdB($A_{\text{e,r}}^{\text{target}}(\boldsymbol{D}_{\text{Low}})$) > 70. Similarly, if PLdB($A_{\text{e,r}}^{\text{target}}(\boldsymbol{D}_{\text{Low}})$) < 70, the overland range can be increased with the corresponding lower cruise altitude such that $\boldsymbol{D}_{\text{MaxR}}$ generated by Eq. (8c) is a plausible low-boom design with 70 PLdB.

The new range maximization formulation [Eq. (8c)] tolerates a wrong choice of the overland mission requirement and avoids solving the multiobjective MDO problem [Eq. (8b)] after a change of the overland mission requirement. This is significantly better than the range maximization formulation [eq. (2f)] in Ref. [41].

The maximum range solution $\boldsymbol{D}_{\text{MaxR}}$ of Eq. (8c) is updated by the solution of Eq. (8d) to satisfy the LTO constraints with the optimal engine thrust. This is also different from the BCO method in Ref. [41], where the engine thrust optimization is independent of the feasibility optimization for the LTO constraints. There are three reasons to combine these two optimization subproblems: 1) the current engine thrust F_s is close to be optimal so it does not have to be optimized before solving Eq. (8b), 2) F_s could have a significant influence on the takeoff field length, and 3) Eq. (8d)

is computationally easy to solve if the LTO constraints are feasible. If the LTO constraints cannot be satisfied by modifying $\boldsymbol{d}_{\mathrm{LTO}}$ and F_{s}, the horizontal tail and wing flaps might have to be redesigned. In practice, the red iteration step involving redesign of the horizontal tail in Fig. 7 needs to be avoided if possible (e.g., reducing the margin in the LTO field length constraints if needed or increasing the wing flap sizes). A significant change of the horizontal tail could lead to a difficult low-boom aft shaping problem [Eq. (8f)], which might have no solution satisfying Eq. (11b). If the LTO constraints are satisfied after solving Eq. (8d) but the engine thrust is changed, then Eq. (8c) might have to be solved again because the weight change at the start of overland cruise might invalidate Eq. (11a). This leads to the inner iteration loop formed by the blue arrow in Fig. 7, which is easy to solve.

   CFD-based low-boom inverse design optimization is only performed for the aft components. In most cases, only one CFD off-body analysis is required to verify whether $\widehat{\boldsymbol{D}}_{\mathrm{MaxR}}$ is a feasible low-boom design. First, Eq. (8e) is solved using CFD surface solutions to enforce $A_{\mathrm{e,CFD}}(l_{\mathrm{e}}, \widehat{\boldsymbol{D}}_{\mathrm{MaxR}}) = A_{\mathrm{e,MuFi}}^{\mathrm{lift}}(l_{\mathrm{e}}, \boldsymbol{D}_{\mathrm{MaxR}})$, which means that the CFD total lift matches the cruise weight of $\boldsymbol{D}_{\mathrm{MaxR}}$ at the start of overland cruise [see Eq. (10)]. If the inverse design optimization criterion [Eq. (11b)], the trim constraint [Eq. (11c)], and $|\widehat{\theta}_{\mathrm{htail}} - \theta_{\mathrm{htail}}| \leq 0.05$ are satisfied for $\widehat{\boldsymbol{D}}_{\mathrm{MaxR}}$, then $\widehat{\boldsymbol{D}}_{\mathrm{MaxR}}$ is a solution of Eq. (4) and the refined BCO method terminates. If $\widehat{\boldsymbol{D}}_{\mathrm{MaxR}}$ does not satisfy Eq. (11b), then Eq. (8f) is solved for $\widehat{\boldsymbol{D}}_{\mathrm{aft}}$ with a low-boom aft shape and the iteration continues. If $\widehat{\boldsymbol{D}}_{\mathrm{MaxR}}$ satisfies Eq. (11b) but violates Eq. (11c), then the parameter δ in Eq. (8a) is reset at a value greater than the current value of $A_{\mathrm{e,r}}^{\mathrm{target}}(l_{\mathrm{e}}/2)/A_{\mathrm{e,r}}^{\mathrm{target}}(l_{\mathrm{e}})$. The baseline low-boom target $A_{\mathrm{e,r,0}}^{\mathrm{target}}$ is regenerated by solving Eq. (8a) and the iteration continues. The last non-termination condition of $|\widehat{\theta}_{\mathrm{htail}} - \theta_{\mathrm{htail}}| > 0.05$ means that the prediction of the CFD tail rotation angle needs to be improved. In this case, usually one additional iteration cycle of solving Eqs. (8b-8e) after another calibration of the low-fidelity aero analyses terminates the refined BCO iteration. It is important to point out that this simplistic approach works for the design study in Sec. III, which starts with a feasible low-boom design. In general, one should start with a large set of design variables for the entire OML to solve Eq. (8f) and use a set of aft design variables to solve Eq. (8f) as $A_{\mathrm{e,MuFi}}$ becomes an accurate approximation of $A_{\mathrm{e,r}}$ in the interval $[0, \lambda]$. The empirical evidence [41] indicates that Eq. (8f) is only needed to be solved once for the entire OML during the BCO iterations.

   Using the multifidelity models, the refined BCO method eliminates the minor wing differences between a plausible low-boom design and a feasible low-boom design generated by the BCO method in Ref. [41]. No convergence theory similar to that in Ref. [50] is available for the refined BCO method. But, in practice, the refined BCO method terminates after a finite number of iteration cycles of solving Eqs. (8a-8f) (see the design study in Sec. III) with the termination conditions in the box connecting to the green oval for the output in Fig. 7.

F. Implementation of Refined BCO Method

   All functions of $\boldsymbol{D}$ used in Eqs. (8a-8d) are computed using the multidisciplinary feasible (MDF) architecture in Fig. 8 (see Ref. [51] for classifications of MDO architectures). The MDF architecture in Fig. 8 is based on the MDO frameworks documented in Refs. [52,53]. The analysis process is similar to that in Ref. [41] and uses the same analysis codes. The main differences are: 1) the low-fidelity aero analyses are performed on the calibrated wing for the truncation parameter $\widehat{y}_{\mathrm{rt}}$, 2) $(\theta_{\mathrm{htail}} - \widehat{\theta}_{\Lambda})$ instead of θ_{htail} is used as the tail rotation angle for low-fidelity aero analyses, and 3) the multifidelity model $A_{\mathrm{e,MuFi}}(\boldsymbol{D})$ [defined by Eqs. (6a-6c)] instead of $A_{\mathrm{e,LoFi}}(\boldsymbol{D})$ is used to define the low-boom inverse design objective for multiobjective MDO.

   An advanced engine model was developed using the Numerical Propulsion System Simulation (NPSS) [54]. This engine model is only scaled by the engine thrust F_{s} in this paper. Equation (8d) can be solved by any derivative-free optimization method (such as the Design Explorer in ModelCenter [55]) if the LTO constraints are feasible. To avoid expensive NPSS runs, an independent copy $\widehat{F}_{\mathrm{s}}$ of F_{s} for NPSS is fixed at the initial value of F_{s} for a baseline configuration and a surrogate model is used during the optimization iterations. The engine size, weight, and performance data are linearly scaled by the surrogate model for any F_{s}. The optimized engine thrust F_{s} is reanalyzed using NPSS to validate the scaling after the optimization. This can be done simply by setting $\widehat{F}_{\mathrm{s}} = F_{\mathrm{s}}$ (of $\boldsymbol{D}$) in Fig. 8, which forces NPSS to regenerate the size, weight, and performance data when the value of $\widehat{F}_{\mathrm{s}}$ is changed.

   The constraints $g_8(\boldsymbol{D}) \geq 0$ and $g_9(\boldsymbol{D}) \geq 0$ [i.e., the range constraints (II.8) and (II.9)] are automatically satisfied with a coupled weight and fixed-range dual-mission analysis method {see the highlighted iteration loop in Fig. 8 and more details in Ref. [40]} using FLOPS [43,44]. The coupled weight and mission analysis generates MTOGW and the weight at the start of overland cruise, along with the component weight and CG$_x$ data. The mission analysis follows the relevant FAA rules for the fuel reserve: 30 min hold at 1500 ft, 5% of total trip fuel, and fuel for 200 nm to alternative airport. Each mission has the following segments: 1) taxi out (9 min), 2) takeoff to 35 ft, 3) climb max 250 kt CAS below 10,000 ft, 4) climb and accelerate to cruise altitude using minimum fuel, 5) cruise at fixed Mach number using optimal altitude (60,000 ft ceiling) for overwater mission or H_{OL} for overland mission, 6) descend at optimal L/D, 7) approach and land (4 min), and 8) taxi in (5 min). This mission profile is based on the one used by Boeing

{see fig. 5.2 in Ref. [5]}. Linear aerodynamics codes WINGDES and AERO2S [56] are used to generate aero data for mission, cruise, and LTO analyses. These aerodynamic analysis codes are applied on the calibrated wing for the truncation parameter $\hat{y}_{rt}$ and the horizontal tail at the calibrated tail rotation angle of $(\theta_{htail} - \hat{\theta}_{\Delta})$. In addition to drag due to lift from WINGDES, skin friction and wave drag coefficients are estimated using the methods in Refs. [57,58], respectively. The SMs are based on the WINGDES/AERO2S centers of pressure and the most aft CG_x values for cruise and LTO weights. For approach velocity and LTO field lengths, the landing weight is 70% of MTOGW and all relevant Part 25 requirements of Federal Aviation Regulations are met [59].
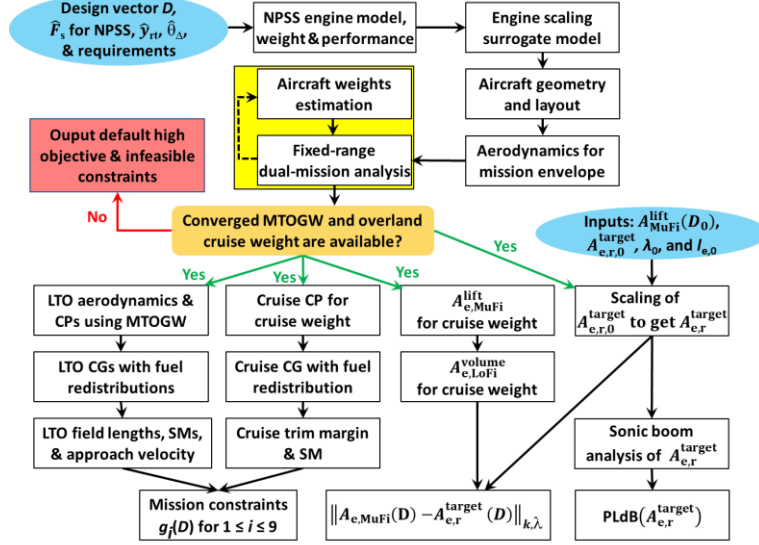
Fig. 8 MDF architecture for analyses of supersonic aircraft concept.

Any equivalent area A_e (including $A_{e,MuFi}$, $A_{e,CFD}$, $A_{e,r}$, $A_{e,r,0}^{target}$, and $A_{e,r}^{target}$) can be converted to an F-function using the following formula [6,7], where $A_e''(t)$ denotes the second derivative of $A_e(t)$.

$$F(x_e) = \frac{1}{2\pi} \cdot \int_0^{x_e} \frac{A_e''(t)}{\sqrt{x_e - t}} dt \tag{13}$$

Then the F-function is converted to a pressure distribution $p(x)$ with $r = 50$ ft using the following equation [8].

$$\frac{p(x_e + r \cdot \beta) - p_\infty}{p_\infty} = \frac{\gamma (M_{OL})^2}{(2 \cdot r \cdot \beta)^{\frac{1}{2}}} \cdot F(x_e) \tag{14}$$

Finally, the solver for an augmented Burgers equation [21] is used to compute the ground signature for A_e by propagating the corresponding p through the standard atmosphere [60] from the altitude $(H_{OL} - 50)$ to the ground. The humidity profile for the standard atmosphere is based on ANSI S1.26 [61]. The method in Ref. [3] is used to compute PLdB of the ground signature.

All CFD results for Eqs. (8e) and (8f) are generated using the Cart3D solver [62] based on three-dimensional Euler equations. The engine shown in Fig. 1 is modeled using a flow-through nacelle for CFD analysis. A volume mesh of about 32 million cells [63] is used for calculation of CFD off-body pressure at 3 body lengths below the aircraft, as well as $CP_{x,CFD}$. The Mach, altitude, and angle of attack for CFD analysis are M_{OL}, H_{OL}, and α of the maximum range solution D_{MaxR} of Eq. (8c). The CFD off-body pressure is used for calculation of $A_{e,r}$ [17].

The positive integer $k = 8$ for the inverse design objective functions in Eqs. (8b) and (8f) provides a good balance for minimizing both maximum and average matching errors. Equations (8a), (8d), (8e), and (8f) are solved using the Design Explorer in ModelCenter [55]. The multiobjective MDO [Eq. (8b)] is solved using the Non-Dominated Sorting Genetic Algorithm II (NSGA II) in ModelCenter. The overland range optimization [Eq. (8c)] is solved only when $|PLdB(A_{e,r}^{target}(D_{Low})) - 69.88| > 0.02$. Equation (8c) is solved with a nested iteration loop: 1) start with $D = D_{Low}$, 2) for a given R_{OL}, change H_{OL} such that the equality constraint for the angle of attack is satisfied (with a tolerance of

0.001°) for D; 3) reduce R_{OL} if PLdB($A_{e,r}^{target}(D)$) – 69.88 > 0.02 and increase R_{OL} if PLdB($A_{e,r}^{target}(D)$) – 69.88 < –0.02, and 4) repeat the previous two steps until |PLdB($A_{e,r}^{target}(D)$) – 69.88| ≤ 0.02.

For an operational computing environment of Windows servers with 40 cores of Intel Xeon CPUs at 2.4 GHz and Linux servers with 96 cores of Intel Xeon CPUs at 2.2 GHz, the average wall-clock time of one iteration cycle for solving Eqs. (8a-8f) is about 2-5 days. It takes about 1-2 days for solving Eq. (8b), 4 hours for solving Eq. (8e) and verifying whether Eqs. (11b-11c) hold, and 1-2 days for solving Eq. (8f) if a feasible low-boom design exists. The refined BCO method usually terminates after a few iteration cycles of solving Eqs. (8a-8f) if no exception occurs. The exceptions include that the horizontal tail has to be resized for the LTO constraints or Eq. (8f) cannot be solved using the simplistic set of the design variables in this paper.

III.   Design Study of Low-Boom Supersonic Transports

For the design study in this paper, the baseline in Sec. II.A is used as the initial $\hat{D}_{aft}$ for the refined BCO method in Fig. 7. Except for the last iteration cycle, λ_0 is the x_e location of the highest point on $A_{e,LoFi}(D_0)$. The engine thrust F_s of 34,000 lb is never changed during the refined BCO iterations. Six iteration cycles of the refined BCO method in Fig. 7 without any LTO constraint violation are performed to get a converged solution $\hat{D}_{MaxR} \approx D_{MaxR}$. The solutions D_{MaxR} and $\hat{D}_{MaxR}$ differ only by a tail rotation angle difference of $\theta_{htail} - \hat{\theta}_{htail} = 0.04°$.

a) Equivalent areas   b) Aft pressure contours
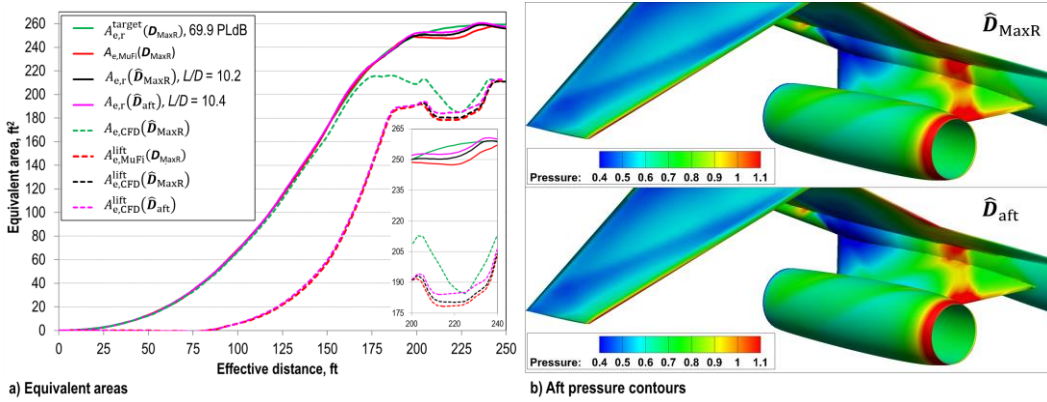
Fig. 9 Optimization results for intermediate low-boom aft shaping solution.
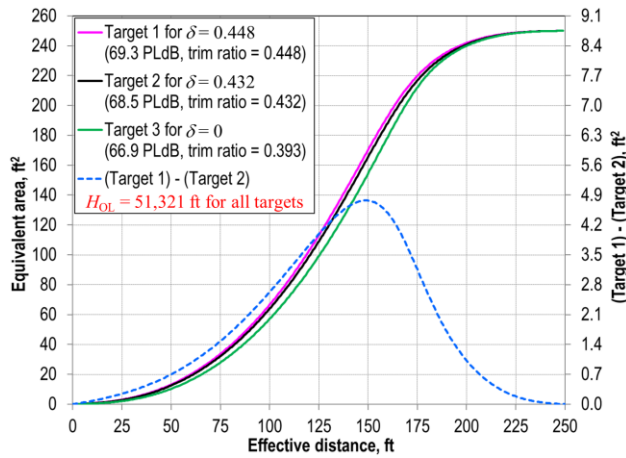
Fig. 10 Low-boom targets for different trim ratios.

Optimization results for an intermediate low-boom aft shaping solution $\hat{D}_{aft}$ of Eq. (8f) are shown in Fig. 9. The calibration parameters $\hat{y}_{rt}$ and $\hat{\theta}_\Delta$ are 1.145 ft and 4.166°, respectively, for the multifidelity models in Sec. II.D. The parameters for the baseline low-boom target are $\mu = 1.227$ and $\delta = 0.438$. The maximum range solution D_{MaxR} has MTOGW of 148,724 lb. The maximum overland range is 3595 nm with H_{OL} of 52,106 ft and the maximum overwater range is 3928 nm (after setting TOGW$_{OW}$ = MTOGW). The angle of attack and the tail rotation angle at the start of overland cruise are 1.92° and 5.04°, respectively. The solution $\hat{D}_{MaxR}$ of Eq. (8e) has a tail rotation angle of 4.92° to

17

match the CFD lift with the weight of D_{MaxR} at the start of overland cruise. The aft shape of $A_{\mathrm{e,r}}(\widehat{D}_{\mathrm{MaxR}})$ is considered to be too far away from the low-boom target (see Fig. 9a). So, Eq. (8f) is solved to get a feasible low-boom design $\widehat{D}_{\mathrm{aft}}$. In this case, $\widehat{D}_{\mathrm{aft}}$ can be obtained from $\widehat{D}_{\mathrm{MaxR}}$ by a change of the incident angle of the pylon with respect to the fuselage from –0.5° to 0.5°. Figure 9a compares the equivalent areas of D_{MaxR}, $\widehat{D}_{\mathrm{MaxR}}$, and $\widehat{D}_{\mathrm{aft}}$, while Fig. 9b compares the aft pressure contours of $\widehat{D}_{\mathrm{MaxR}}$ and $\widehat{D}_{\mathrm{aft}}$. Note that $A_{\mathrm{e,MuFi}}(D_{\mathrm{MaxR}})$ is an accurate prediction of $A_{\mathrm{e,r}}(\widehat{D}_{\mathrm{MaxR}})$ except some noticeable differences in the aft region.
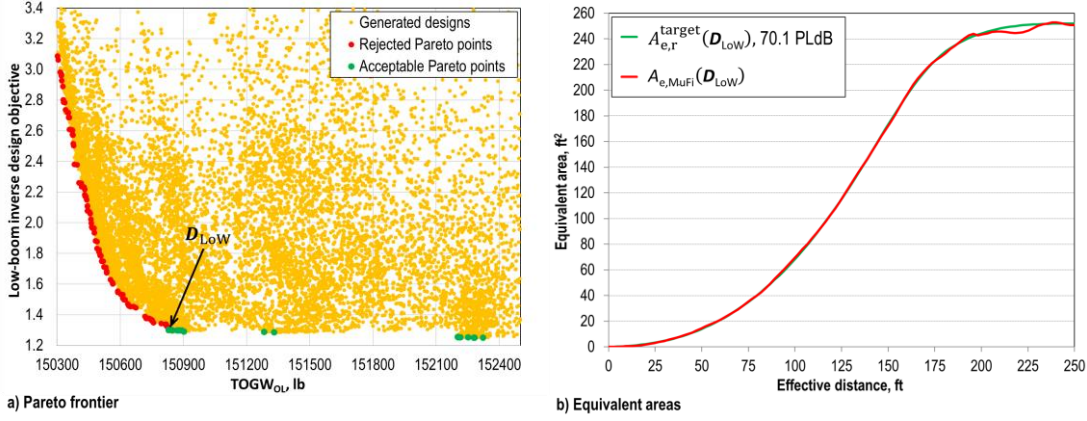
Fig. 11 Pareto frontier and equivalent areas for D_{LoW}.

For the last iteration cycle of the refined BCO method, the calibration parameters $\hat{y}_{\mathrm{rt}}$ and $\widehat{\theta}_{\Delta}$ are 1.270 ft and 3.803°, respectively. The CFD correction terms for the multifidelity A_{e} models are plotted in Fig. 5. The optimal R_{OL} and H_{OL} from the previous iteration cycle are 3695 nm and 51,321 ft, respectively, which define the overland range constraint $g_9(D) \geq 0$ for Eq. (8b). The baseline low-boom target is generated using $\mu = 1.215$ and $\delta = 0.448$. Figure 10 compares the baseline low-boom targets for $\delta = 0$, 0.432 (used for $\widehat{D}_{\mathrm{LoT}}$ in Ref. [41]), and 0.448 when $H_{\mathrm{OL}} = 51,321$ ft, $l_{\mathrm{e,0}} = 249$ ft, and $A_{\mathrm{e,r,0}}^{\mathrm{target}}(l_{\mathrm{e,0}}) = 250$ ft². Note that the trim ratio $A_{\mathrm{e,r}}^{\mathrm{target}}(l_{\mathrm{e}}/2)/A_{\mathrm{e,r}}^{\mathrm{target}}(l_{\mathrm{e}})$ equals δ if δ is large enough to make the midpoint constraint in Eq. (8a) active. A total of 13,300 designs are generated by NSGA II in ModelCenter with a population size of 100 for each generation. The fixed-range dual mission analysis failed for 238 designs. For each failed case, high objective and infeasible constraint values (see the red box in Fig. 8) are used to steer the optimizer away from the design with failed mission analysis. The Pareto frontier for Eq. (8b) and the A_{e} analysis results for D_{LoW} are shown in Fig. 11. The Pareto frontier is partitioned into two groups: the rejected designs that violate the inverse design matching error constraint Eq. (11a) and the acceptable designs that satisfy Eq. (11a). The selected Pareto solution for Eq. (8b) is labeled as D_{LoW} that is the acceptable design with the lowest weight. Figure 11b shows that D_{LoW} is a plausible low-boom design with 70.1 PLdB, which is higher than 70 PLdB.
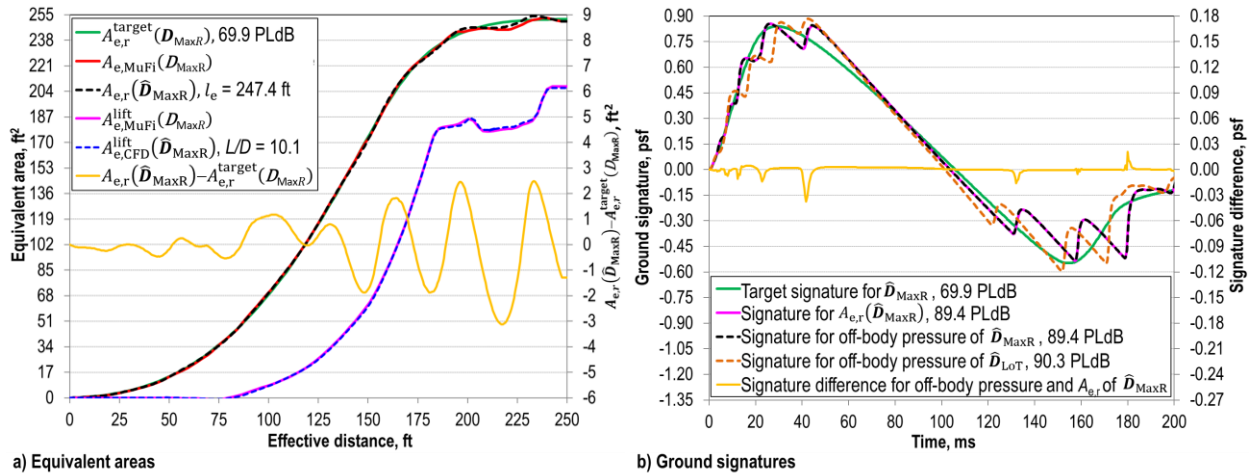

Fig. 12 Equivalent areas of D_{MaxR} and $\widehat{D}_{\mathrm{MaxR}}$, and signatures for $\widehat{D}_{\mathrm{MaxR}}$ and $\widehat{D}_{\mathrm{LoT}}$.

When using Eq. (8c) to get a plausible low-boom design D_{MaxR} with 69.9 PLdB from D_{LoW}, R_{OL} is reduced from 3695 nm to 3500 nm and H_{OL} is increased from 51,321 ft to 52,240 ft. The angle of attack and the tail rotation angle at the start of overland cruise for D_{MaxR} are 2.30° and 4.61°, respectively, which are the same as those for D_{LoW}. The solution D_{MaxR} has MTOGW of 144,251 lb and a zero fuel weight of 70,842 lb. After setting TOGW$_{\text{OW}}$ = MTOGW, the maximum overwater range of D_{MaxR} is increased from 3600 nm to 3882 nm. It is worth noting that the calibrated lift method usually leads to a higher drag at the start of cruise than that from the original low-fidelity aero analysis. For D_{MaxR}, the total of wave drag and induced drag using the calibrated wing is 0.00792, higher than 0.00764 for using the original wing, at the start of low-boom cruise.

a) Fuselage

b) Planform

c) Airfoils
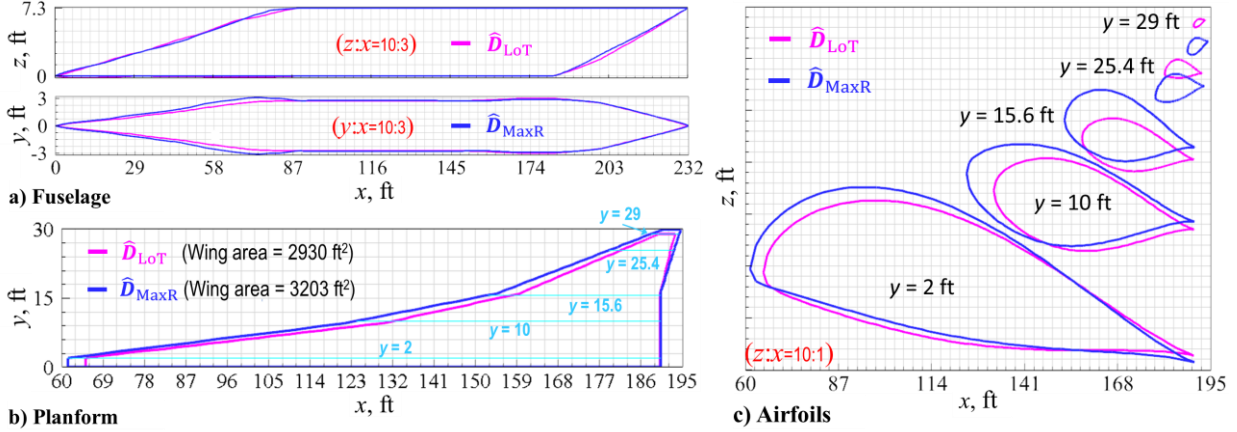
Fig. 13 Fuselage and wing shapes of $\widehat{D}_{\text{MaxR}}$ and $\widehat{D}_{\text{LoT}}$.

The solution $\widehat{D}_{\text{MaxR}}$ of Eq. (8e) has a slightly different tail rotation angle of 4.57°. Figure 12a shows that $A_{\text{e,MuFi}}(D_{\text{MaxR}})$ is an accurate prediction of $A_{\text{e,r}}(\widehat{D}_{\text{MaxR}})$ with minor differences in the aft region and $A_{\text{e,r}}(\widehat{D}_{\text{MaxR}})$ matches the low-boom target closely. The feasible low-boom design $\widehat{D}_{\text{MaxR}}$ has a shaped ground signature oscillating along the low-boom target signature (see Fig. 12b). Moreover, $\widehat{D}_{\text{MaxR}}$ has a trim margin of CG$_{x,\text{aft}}$ − CP$_{x,\text{CFD}}$ = 169.5 − 167.6 = 1.9 ft and satisfies Eq. (11c). So, the refined BCO method terminates with $|\theta_{\text{htail}} - \hat{\theta}_{\text{htail}}| = 4.61 - 4.57 = 0.04 < 0.05$. The following mission constraint values for $\widehat{D}_{\text{MaxR}}$ satisfy the constraints (II.1)-(II.6).

(III.1) CG margin to prevent tip over on the ground is 12.6 ft.
(III.2) SM for overland cruise = 6.5% of MAC.
(III.3) LTO SMs are 4.8% and 2% of MAC, respectively.
(III.4) Tail rotation angles for trim at LTO are −15.2° and −14.9°, respectively.
(III.5) LTO field lengths are 6742 ft and 8320 ft, respectively.
(III.6) Approach velocity = 136 kt at altitude of 1000 ft.

The fuselage and wing shapes of $\widehat{D}_{\text{MaxR}}$ are compared with those of $\widehat{D}_{\text{LoT}}$ in Ref. [41] (see Fig. 13). The widths of front fuselage of $\widehat{D}_{\text{LoT}}$ are increased and the wing of $\widehat{D}_{\text{LoT}}$ is extended forward for $\widehat{D}_{\text{MaxR}}$ to match $A_{\text{e,r}}^{\text{target}}(D_{\text{MaxR}})$. The surface pressure contour of $\widehat{D}_{\text{MaxR}}$ is shown in Fig. 14, which is visually similar to that of $\widehat{D}_{\text{LoT}}$ {see fig. 16 in Ref. [41]}, and the Euler L/D at the start of overland cruise for $\widehat{D}_{\text{MaxR}}$ is 10.1, about 13.5% higher than the Euler L/D of 8.9 for $\widehat{D}_{\text{LoT}}$. In comparison, the low-fidelity L/D of D_{MaxR} including the skin friction drag is 7.73 at the start of overland cruise.
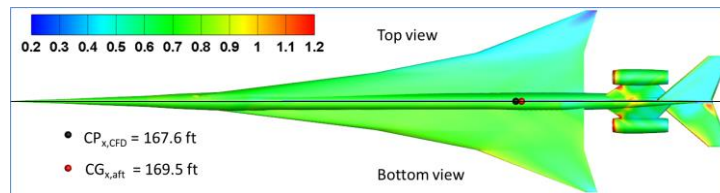

Fig. 14 CFD pressure contour for $\widehat{D}_{\text{MaxR}}$ at start of overland cruise.

It is important to note that the potential to achieve the target PLdB value of 69.9 for a feasible low-boom design is yet to be realized with future development of low-boom shaping methods to tailor the ground signature for a significantly lower PLdB. As pointed out before, the current CFD-based low-boom inverse design methods [17,22-

19

25] are capable of using local shape modifications to lower the noise level of the undertrack ground signature below 79 PLdB. How to narrow the gap between the target PLdB value and the actual PLdB value of the undertrack ground signature of the optimal low-boom inverse design is still an open problem in CFD-based low-boom inverse design optimization. Another issue related to the fidelity of the generated low-boom concept in this paper is the use of a flow-through nacelle to model the engine. A low-boom configuration with a flow-through nacelle usually loses its low-boom characteristics once the flow-through nacelle is replaced by a powered engine. See Ref. [24] for a detailed discussion about how the powered engine simulation could affect the low-boom design. Furthermore, only the noise level in PLdB for the undertrack ground signature at the start of overland cruise is considered in this paper. In reality, a commercial supersonic transport must satisfy the specified low-boom requirement (that is the upper limit of 70 PLdB in this paper) for its sonic boom ground noise levels in all directions (not just the undertrack direction) under the entire flight trajectory. This is still an unsolved problem for future research.

IV. Conclusions

A CFD-based multiobjective MDO problem is formulated for development of low-boom supersonic transports. For every design, the mission analysis is calibrated using one CFD analysis so that the wing lift and total lift generated by the low-fidelity aero analysis code are nearly identical to the CFD wing lift and total lift at the start of overland cruise. The multifidelity mission analysis eliminates the inconsistency between CFD analysis for low-boom inverse design optimization and low-fidelity aero analyses for multiobjective MDO with the mission constraints.

Multifidelity models for the mission performance metrics and CFD equivalent areas are constructed to solve the CFD-based multiobjective MDO problem. The previous block coordinate optimization (BCO) method is refined to improve the low-boom cruise efficiency and increase the fidelity of MDO solutions. For a given low-boom cruise Mach, the refined BCO method can generate a low-boom supersonic transport that satisfies the mission performance requirements and has the potential to achieve an undertrack sonic boom ground noise level below 70 PLdB. The details for the generated low-boom supersonic transport are summarized in Table 4. This concept demonstrates that the NASA N+3 low-boom goal for a supersonic transport with ground noise level below 70 PLdB might be achievable.

Table 4 Low-boom supersonic transport generated by the refined BCO method

Number of passengers	40	Overwater cruise Mach	1.8
Seat pitch, in	48	Overwater range, nm	3882
Fuselage length, ft	232	Low-boom cruise Mach	1.7
Wingspan, ft	60	Low-boom range, nm	3500
Wing area, ft^2	3203	Low-boom cruise altitude, ft	52,240
MTOGW, lb	144,251	PLdB of inverse design target	69.9
Zero fuel weight, lb	70,842	Euler CFD L/D for low-boom cruise	10.1
Maximum LTO field length, ft	8320	Low-fidelity L/D for low-boom cruise	7.7
Approach velocity, kt	136	CFD trim margin for low-boom cruise, ft	1.9

Acknowledgments

References

[1] Pawlowski, J., Graham, D., Boccadoro, C., Coen, P., and Maglieri, D., "Origins and Overview of the Shaped Sonic Boom Demonstration Program," AIAA Paper 2005-5, January 2005. doi:10.2514/6.2005-5

[2] "Low-Boom Flight Demonstrator Project," NASA Aeronautics Mission Directorate, URL: https://www.nasa.gov/aeroresearch/programs/iasp/lbfd [retrieved 2 June 2021].

[3] Stevens, S., "Perceived Level of Noise by Mark VII and Decibels (E)," *Journal of the Acoustical Society of America*, Vol. 51, No. 2B, 1972, pp. 575–601. doi:10.1121/1.1912880

[4] Morgenstern, J., Norstrud, N., Stelmack, M., and Jha, P., "Advanced Concept Studies for Supersonic Commercial Transports Entering Service in 2030-2035 (N+3)," AIAA Paper 2010-5114, June 2010. doi:10.2514/6.2010-5114

[5] Welge, H., Bonet, J., Magee, T., Tompkins, D., Britt, T., Nelson, C., Miller, G., Stenson, D., Staubach, J., Bala, N., Duge, R., O'Brien, M., Cedoz, R., Barlow, A., Martins, S., Viars, P., Rasheed, A., Kirby, M., Raczynski, C., Roughen, K., Doyle, S.,

Alston, K., Page, J., and Plotkin, K., "N+3 Advanced Concept Studies for Supersonic Commercial Transport Aircraft Entering Service in the 2030-2035 Period," NASA CR-2011-217084, April 2011.

[6] Whitham, G., "The Flow Pattern of a Supersonic Projectile," *Communications on Pure and Applied Mathematics*, Vol. 5, No. 3, 1952, pp. 301–348. doi:10.1002/cpa.3160050305

[7] Walkden, F., "The Shock Pattern of a Wing-Body Combination, Far from the Flight Path," *Aeronautical Quarterly*, Vol. 9, No. 2, 1958, pp. 164–194. doi:10.1017/S0001925900001372

[8] Seebass, R., and George, A., "Sonic Boom Minimization," *Journal of the Acoustical Society of America*, Vol. 51, No. 2C, 1972, pp. 686–694. doi:10.1121/1.1912902

[9] Darden, C., "Sonic-Boom Minimization with Nose-Bluntness Relaxation," NASA TP-1348, January 1979.

[10] Rallabhandi, S., and Mavris, D., "Aircraft Geometry Design and Optimization for Sonic Boom Reduction," *Journal of Aircraft*, Vol. 44, No. 1, 2007, pp. 35–47. doi:10.2514/1.20456

[11] Plotkin, K., Rallabhandi, S., and Li, W., "Generalized Formulation and Extension of Sonic Boom Minimization Theory for Front and Aft Shaping," AIAA Paper 2009-1052, January 2009. doi:10.2514/6.2009-1052

[12] Haas, A., and Kroo, I., "A Multi-Shock Inverse Design Method for Low-Boom Supersonic Aircraft," AIAA Paper 2010-843, June 2010. doi:10.2514/6.2010-843

[13] Morgenstern, J., "Optimum Signature Shaping for Low Sonic Boom," AIAA Paper 2012-3218, June 2012. doi: 10.2514/6.2012-3218

[14] Kasuga, Y., and Yoshida, K., "A New F-Function for the Low-Boom Aircraft Design with Trim Requirement," AIAA Paper 2016-2032, January 2016. doi:10.2514/6.2016-2032

[15] Minelli, A., Salah el Din, I., and Carrier, G., "Inverse Design Approach for Low-Boom Supersonic Configurations," *AIAA Journal*, Vol. 52, No. 10, 2014, pp. 2198–2212. doi:10.2514/1.J052834

[16] Maglieri, D., Bobbitt, P., Plotkin, K., Shepherd, K., Coen, P., and Richwine, D., *Sonic Boom: Six Decades of Research*, NASA SP-2014-622, NASA Langley Research Center, 2014.

[17] Li, W., and Rallabhandi, S., "Inverse Design of Low-Boom Supersonic Concepts Using Reversed Equivalent-Area Targets," *Journal of Aircraft*, Vol. 51, No. 1, 2014, pp. 29–36. doi:10.2514/1.C031551

[18] Park, M., and Carter, M., "Nearfield Summary and Analysis of the Third AIAA Sonic Boom Prediction Workshop C608 Low Boom Demonstrator," AIAA Paper 2021-0345, Jan. 2021. doi:10.2514/6.2021-0345

[19] Rallabhandi, S., and Loubeau, A., "Summary of Propagation Cases of the Third AIAA Sonic Boom Prediction Workshop," AIAA Paper 2021-0229, Jan. 2021. doi:10.2514/6.2021-0229

[20] Cleveland, R., Chambers, J., Bass, H., Raspet, R., Blackstock, D., and Hamilton, M., "Comparison of Computer Codes for the Propagation of Sonic Boom Waveforms Through Isothermal Atmospheres," *Journal of the Acoustical Society of America*, Vol. 100, No. 5, 1996, pp. 3017–3027. doi:10.1121/1.417113

[21] Rallabhandi, S., "Advanced Sonic Boom Prediction Using Augmented Burgers Equation," *Journal of Aircraft*, Vol. 48, No. 4, 2011, pp. 1245–1253. doi:10.2514/1.C031248

[22] Aftosmis, M., Nemec, M., and Cliff, S., "Adjoint-Based Low-Boom Design with Cart3D," AIAA Paper 2011-3500, June 2011. doi:10.2514/6.2011-3500

[23] Rallabhandi, S., "Application of Adjoint Methodology to Supersonic Aircraft Design Using Reversed Equivalent Areas," *Journal of Aircraft*, Vol. 51, No. 6, 2014, pp. 1873–1882. doi:10.2514/1.C032518

[24] Wintzer, M., Ordaz, I., and Fenbert, J., "Under-Track CFD-Based Shape Optimization for a Low-Boom Demonstrator Concept," AIAA Paper 2015-2260, June 2015. doi:10.2514/6.2015-2260

[25] Li, W., "Feasibility of Supersonic Aircraft Concepts for Low-Boom and Flight Trim Constraints," AIAA Paper 2015-2581, June 2015. doi:10.2514/6.2015-2581

[26] Ueno, A., Kanamori, M., and Makino, Y., "Multi-Fidelity Low-Boom Design Based on Near-Field Pressure Signature," AIAA Paper 2016-2033, January 2016. doi:10.2514/6.2016-2033

[27] Wlezien, R., and Veitch, L., "Quiet Supersonic Platform Program," AIAA Paper 2002-143, Jan. 2002. doi:10.2514/6.2002-143

[28] Brezillon, J., Carrier, G., and Laban, M., "Multidisciplinary Optimization of Supersonic Aircraft Including Low-Boom Considerations," *Journal of Mechanical Design*, Vol. 133, No. 10, 105001, October 2011. doi:10.1115/1.4004972

[29] Sun, Y., and Smith, H., "Low-Boom Low-Drag Optimization in a Multidisciplinary Design Analysis Optimization Environment," *Aerospace Science and Technology*, Vol. 94, 105387, November 2019. doi:10.1016/j.ast.2019.105387

[30] Feng, X., Li, Z., and Song, B., "Research of Low Boom and Low Drag Supersonic Aircraft Design," *Chinese Journal of Aeronautics*, Vol. 27, No. 3, 2014, pp. 531–541. doi:10.1016/j.cja.2014.04.004

[31] Ban, N., Yamazaki, W., and Kusunose, K., "Low-Boom/Low-Drag Design Optimization of Innovative Supersonic Transport Configuration," *Journal of Aircraft*, Vol. 55, No. 3, 2018, pp. 1071–1081. doi:10.2514/1.C034171

[32] Sato, K., Kumano, T., Yonezawa, M., Yamashita, H., Jeong, S., and Obayashi, S., "Low-Boom and Low-Drag Optimization of the Twin Engine Version of Silent Supersonic Business Jet," *Journal of Fluid Science and Technology*, Vol. 3, No. 4, 2008, pp. 576–585. doi:10.1299/jfst.3.576

[33] Chiba, K., Makino, Y., and Takatoya, T., "Evolutionary-Based Multidisciplinary Design Exploration for Silent Supersonic Technology Demonstrator Wing," *Journal of Aircraft*, Vol. 45, No. 5, 2008, pp. 1481–1494. doi:10.2514/1.33272

[34] Chiba, K., Makino, Y. and Takatoya, T., "Design-Informatics Approach for Intimate Configuration of Silent Supersonic Technology Demonstrator," *Journal of Aircraft*, Vol. 49, No. 5, 2012, pp.1200–1211. doi:10.2514/1.C031116

[35] Kanazaki, M., and Seto, N., "Efficient Global Optimization Applied to Design and Knowledge Discovery of Supersonic Wing," *Journal of Computational Science and Technology*, Vol. 6, No. 1, 2012, pp. 1–15.

[36] Choi, S., Alonso, J., Kroo, I., and Wintzer, M., "Multifidelity Design Optimization of Low-Boom Supersonic Jets," *Journal of Aircraft*, Vol. 45, No. 1, 2008, pp. 106–118. doi:10.2514/1.28948

[37] Alonso, J., and Colonno, M., "Multidisciplinary Optimization with Applications to Sonic-Boom Minimization," *Annual Review of Fluid Mechanics*, Vol. 44, January 2012, pp. 505–526. doi:10.1146/annurev-fluid-120710-101133

[38] Makino, Y., Suzuki, K., Noguchi, M., and Yoshida, K., "Nonaxisymmetrical Fuselage Shape Modification for Drag Reduction of Low-Sonic-Boom Airplane," *AIAA Journal*, Vol. 41, No. 8, 2003, pp. 1413–1420. doi:10.2514/2.2109

[39] Lukaczyk, T., Palaciosy, F., and Alonso, J., "Response Surface Methodologies for Low-Boom Supersonic Aircraft Design using Equivalent Area Distributions," AIAA Paper 2012-5705, September 2012. doi:10.2514/6.2012-5705

[40] Li, W., and Geiselhart, K., "Multidisciplinary Design Optimization of Low-Boom Supersonic Aircraft with Mission Constraints," *AIAA Journal*, Vol. 59, No. 1, 2021, pp. 165–179. doi:10.2514/1.J059237

[41] Li, W., and Geiselhart, K., "Integration of Low-Fidelity MDO and CFD-Based Redesign of Low-Boom Supersonic Transports," *AIAA Journal*, Vol. 59, No. 10, 2021, pp. 3923–3936. doi:10.2514/1.J060368

[42] Ordaz, I., and Li, W., "Approximation of Off-Body Sonic-Boom Analysis for Low-Boom Conceptual Design," *Journal of Aircraft*, Vol. 53, No. 1, 2016, pp. 14–19. doi:10.2514/1.C033159

[43] Carlson, H., and Mack, R., "Estimation of Wing Nonlinear Aerodynamic Characteristics at Supersonic Speeds," NASA TP-1718, November 1980.

[44] Ladson, C., Brooks, C., Jr., Hill, A., and Sproles, D., "Computer Program to Obtain Ordinates for NACA Airfoils," NASA TM-1996-4741, December 1996.

[45] Peherstorfer, B., Willcox, K., and Gunzburger, M., "Survey of Multifidelity Methods in Uncertainty Propagation, Inference, and Optimization," *SIAM Review*, Vol. 60, No. 3, 2018, pp. 550–591. doi:10.1137/16M1082469

[46] Viana, F., Simpson, T., Balabanov, V., and Toropov, V., "Metamodeling in Multidisciplinary Design Optimization: How Far Have We Really Come?" *AIAA Journal*, Vol. 52, No. 4, 2014, pp. 670–690. doi:10.2514/1.J052375

[47] McCullers, L., *FLOPS User's Guide*, NASA Langley Research Center, Hampton, Virginia, 2011 (available with public distribution of software).

[48] Wells, D., Horvath, B., and McCullers, L., "The Flight Optimization System Weights Estimation Method," NASA TM-2017-219627, Volume 1, January 2017.

[49] Renganathan, S., "Koopman-Based Approach to Nonintrusive Reduced Order Modeling: Application to Aerodynamic Shape Optimization and Uncertainty Propagation," *AIAA Journal*, Vol. 58, No. 5, 2020, pp. 2221–2235. doi:10.2514/1.J058744

[50] March, A., and Willcox, K., "Provably Convergent Multifidelity Optimization Algorithm Not Requiring High-Fidelity Derivatives," *AIAA Journal*, Vol. 50, No. 5, 2012, pp. 1079–1089. doi:10.2514/1.J051125

[51] Martins, J., and Lambe, A., "Multidisciplinary Design Optimization: a Survey of Architectures," *AIAA Journal*, Vol. 51, No. 9, 2013, pp. 2049–2075. doi:10.2514/1.J051895

[52] Ozoroski, L., Geiselhart, K., Padula, S., Li, W., Olson, E., and Campbell, R., "Initial Multidisciplinary Design and Analysis Framework," NASA TM-2010-216711, June 2010.

[53] Geiselhart, K., Ozoroski, L., Fenbert, J., Shields, E., and Li, W., "Integration of Multifidelity Multidisciplinary Computer Codes for Design and Analysis of Supersonic Aircraft," AIAA Paper 2011-0465, January 2011. doi:10.2514/6.2011-465

[54] *Numerical Propulsion System Simulation (NPSS), Version 2.8*, Southwest Research Institute, URL:https://www.swri.org/consortia/numerical-propulsion-system-simulation-npss [retrieved 2 June 2021].

[55] *ModelCenter, Version 12.0*, Phoenix Integration Inc., URL:http://www.phoenix-int.com [retrieved 2 June 2021].

[56] Carlson, H., Chu, J., Ozoroski, L., and McCullers, L., "Guide to AERO2S and WINGDES Computer Codes for Prediction and Minimization of Drag Due to Lift," NASA TP-3637, November 1997.

[57] Sommer, S., and Short, B., "Free-Flight Measurements of Turbulent-Boundary-Layer Skin Friction in the Presence of Severe Aerodynamic Heating at Mach Numbers from 2.8 to 7.0," NACA TN-3391, 1955.

[58] Harris, R., Jr., "An Analysis and Correlation of Aircraft Wave Drag," NASA TM X-947, March 1964.

[59] McCullers, L., *FLOPS User's Guide for Detailed Takeoff and Landing Analysis Program*, NASA Langley Research Center, Hampton, Virginia, 2008 (available with public distribution of software).

[60] *U.S. Standard Atmosphere, 1976*, U.S. Government Printing Office, Washington, D.C., 1976. URL: https://www.ngdc.noaa.gov/stp/space-weather/online-publications/miscellaneous/us-standard-atmosphere-1976/us-standard-atmosphere_st76-1562_noaa.pdf [retrieved 26 June 2021].

[61] *Method for Calculation of the Absorption of Sound by the Atmosphere, Annex C*, American National Standards Inst., Standard S1.26-1995, New York, 1995.

[62] Aftosmis, M., Berger, M., and Melton, J., "Robust and Efficient Cartesian Mesh Generation for Component-Based Geometry," *AIAA Journal*, Vol. 36, No. 6, 1998, pp. 952–960. doi:10.2514/2.464

[63] Ordaz, I., and Li, W., "Integration of Off-Track Sonic Boom Analysis for Supersonic Aircraft Conceptual Design," *Journal of Aircraft*, Vol. 51, No. 1, 2014, pp. 23–28. doi:10.2514/1.C031511